Deep–Sea Research I xxx (xxxx) xxx

Contents lists available at ScienceDirect

Deep-Sea Research Part I

journal homepage: http://www.elsevier.com/locate/dsri

A Fukushima tracer perspective on four years of North Pacific mode water evolution

Alison M. Macdonald [a,*], Sachiko Yoshida [a], Steven M. Pike [b], Ken O. Buesseler [b], Irina I. Rypina [a], Steven R. Jayne [a], Vincent Rossi [c,d], Jennifer Kenyon [b], Jessica A. Drysdale [b]

[a] Woods Hole Oceanographic Institution, Physical Oceanography Department, Woods Hole, MA, USA
[b] Woods Hole Oceanographic Institution, Marine Chemistry and Geochemistry Department, Woods Hole, MA, USA
[c] Mediterranean Institute of Oceanography (UM 110, UMR 7294), CNRS, Aix Marseille Univ., Univ. Toulon, IRD, Marseille, 13288, France
[d] Climate Change Research Centre, University of New South Wales, Sydney, New South Wales, 2052, Australia

ARTICLE INFO

Keywords:
Fukushima radiocesium
Mode water
North Pacific
Radionuclide tracer
Ocean circulation

ABSTRACT

We present the results of a multi-platform investigation that utilizes tracer information provided by the 2011 release of radioisotopes from the Fukushima Dai-ichi Nuclear Power Plant to better understand the pathways, mixing and transport of mode waters formed in the North Pacific Ocean. The focus is on transition region mode waters and radiocesium (^{137}Cs and ^{134}Cs) observations obtained from the May–June 2015 GO-SHIP occupation of the 152°W line in the Northeast Pacific. Samples include profiles from the surface to 1000 m and surface/subsurface pairs that provide an average 1° of latitude spacing along 152°W. We find a clear Fukushima (^{134}Cs) signal from the surface to 400 m. The core signal (^{134}Cs ~10 Bq m^{-3}, ^{137}Cs ~12 Bq m^{-3}) at 41°-43°N lies at 30–220 m where mode waters formed through deep winter mixing in 2011 outcropped in the western North Pacific. The strongest 2015 152°W Fukushima-source radiocesium signal is associated with Dense-Central Mode Waters consistent with the densest variety of these mode waters being formed off the coast of Japan 4 years earlier. The radionuclide signal transited the basin along subsurface mode water isopycnals mainly on the northern side of the subtropical gyre before outcropping at and to the east of the 152°W line. In 2015, the densest 152°W waters with ^{134}Cs lie at ~435 m in the bottom range of Dense-Central Mode Water at 40°N. There is a weak, but detectable, signal in the boundary current off both Kodiak and Sitka. The deepest detectable ^{137}Cs (weapon's testing background) are found at and to the north of 45°N at 900–1000 m. With the exception of a single subsurface sample near Hawaii, as of spring 2015, the southernmost ^{134}Cs was found above 200 m at 30°N. A total date-corrected ^{134}Cs inventory of 11–16 PBq is estimated. Qualitative comparison to model output suggests good consistency in terms of general location, latitudinal breadth, and predicted depth of penetration, allowing discussion of the bigger picture. However, the model's 2015 152°W radiocesium signal is quantitatively weaker and the core is offset in latitude, potentially due to the lack of consideration of atmospheric deposition.

1. Introduction

In the Northwest Pacific, warm tropical/subtropical waters meet cold, upwelled, nutrient rich waters from the north in a confluence zone east of Japan. Here, a variety of mode waters are formed in deep winter mixed layers, reaching 300–400 m. It is also here that the radionuclide contamination from the 2011 Fukushima Dai-ichi Nuclear Power Plant (FDNPP) accident was directly discharged into the ocean and where the major portion of the atmospheric deposition was thought to have occurred. This study examines the spread of Northwest Pacific mode water (MW) from the perspective of observations made 4 years after the accident along 152°W and in the Alaska Gyre. While many different radioisotopes were released as a result of the 2011 accident, we focus on radiocesium (henceforth referred to as Cs), in particular ^{137}Cs (30.07-year half-life) and ^{134}Cs (2.06-year half-life). Although the Pacific Ocean has received Cs input in the past, most notably due to nuclear weapons testing during the 1950's and 60's, given its two-year half-life, the presence of ^{134}Cs is a unique diagnostic tool for indicating the presence of waters derived from the FDNPP. Henceforth, water tagged with ^{134}Cs will be referred to as FDNPP Cs or simply Cs_F. The Cs_F release afforded

* Corresponding author. WHOI MS21, 266 Woods Hole Rd., Woods Hole, MA 02543.
E-mail address: amacdonald@whoi.edu (A.M. Macdonald).

https://doi.org/10.1016/j.dsr.2020.103379
Received 28 February 2019; Received in revised form 26 August 2020; Accepted 27 August 2020
Available online 2 September 2020
0967-0637/© 2020 Elsevier Ltd. All rights reserved.

an opportunity to employ a powerful, soluble, readily detectable tracer input to the ocean at a known time and location to better understand the timing and spread of North Pacific MW.

Section 1 includes a review of North Pacific circulation and mode waters, and a short history of North Pacific Cs. Section 2 presents the Northeast Pacific observed Cs dataset and its distribution. Section 3 relates the observed Cs patterns with MW distributions, calculates inventories, brings ^{90}Sr estimates to bear and compares the observations to model predictions. Section 4 is a summary. Throughout, radionuclide units are given as activity in Bq (1 Bq = 1 nucleus decay per second) and activity concentration Bq m^{-3}.

1.1. North Pacific circulation and mode waters

North Pacific surface circulation is composed of three wind driven gyres: one subtropical and two semi-distinct subpolar, the Alaska and Western Sub-arctic Gyres (Fig. 1). The western boundary Kuroshio Current separates from the coast at ~35°N as it turns into the open ocean. Bifurcating, the main portion flows east as a strong inertial jet known as the Kuroshio Extension (KE), and slightly further north, influenced by Oyashio waters, the Kuroshio Bifurcation Front (KBF) extends eastward to become the Subarctic Current (Oka and Qiu, 2012).

In the west, to the south of the frontal regions (KE Front, KBF and further north near the Subarctic Front) strong heat loss to the atmosphere results in vertical convective mixing in winter. These regions of deep mixing have been illustrated by February mixed layer depths (MLD) observed by historical hydrography (Talley, 1988; Suga et al., 2004), satellites (e.g. Fig. 1) and profiling floats (e.g. Whalen et al. (2012); Yoshida et al. (2015)). The resulting ventilated, low potential vorticity "mode" waters that lie slightly above or within the permanent pycnocline are classified into six classes according to their distinct but homogeneous hydrodynamical characteristics (Table 1) and are reviewed in detail by Oka and Qiu (2012).

North Pacific Subtropical Mode Water (STMW $24.5 < \sigma_0 < 25.9$) is formed to the south of the KE front, and is associated with deep mixed layers (up to 400–450 m) and the anticyclonic recirculation of the Kuroshio Current system (e.g.Suga and Hanawa, 1995; Qiu et al., 2006). STMW's low potential vorticity is thought to arise largely through lateral induction (i.e. advection across a changing MLD) supported by the strong mixed layer front found on the southern flank of the formation region, which is characterized by large surface density gradients (Suga et al., 2004).

Transition Region and Dense-Central Mode Waters (TRMW $26.3 < \sigma_0 < 26.6$, D-CMW, $25.9 < \sigma_0 < 26.9$) are formed to the north of the KBF and to the south of the polar fronts as a zonal band of deep winter mixed layers emanating from the west coast of Japan (39–43°N) and extending beyond 160°W (Oka et al., 2011). *Light Central Mode Water* (L-CMW, $25.5 < \sigma_0 < 26.3$) is formed between the KE and the KBF in regions of moderate (150–225 m) mixed layers that do not change significantly along isopycnals, where there is little diapycnal flow (Suga et al., 2004) and zonal surface density gradients are small.

Central Mode Water (CMW) that is formed to the west of 170°E cannot be subducted into the permanent pycnocline due to the deeper and lighter mixed layers found downstream. However, CMW formed to the east of this longitude, where downstream winter mixed layers are shoaling, can be, and therefore, can also be advected into the anticyclonic circulation of the subtropical gyre (Oka et al., 2011). This picture is complicated by dedacal-scale shifts in fronts and mesocale eddy activity linked to changes is surface wind forcing that can affect CMW formation (e.g. Oka and Qiu, 2012 and references therein; Kawakami et al., 2016). The possible effects of CMW formation variability include impacts on oxygen utilization rates (Kwon et al., 2016), carbon uptake and storage rates, and sea-surface temperatures. While interannual variations (Kawakami et al., 2016) and formation region eddy activity (Dong et al., 2017) are now being studied using Argo and satellite records, less is understood about longer timescale variations and effects outside formation regions.

Eastern Subtropical Mode Water (ESTMW $23.9 < \sigma_0 < 26.1$) is by definition formed to the east of the dateline. While ESTMW forms in regions with fairly shallow MLDs (100–140 m, Katsura, 2018), which are somewhat less homogeneous along isopycnals than those of CMW, compensating gradients in a fairly broad range of SSS and SST are responsible for minimal density gradients, so as for CMW, low potential vorticity is achieved through to lack of diapycnal flow (Suga et al.,

Table 1
North Pacific Mode Water temperature, salinity and density characteristic definitions used for this study. TRMW definition comes from Saito et al. (2011). All others come from Bingham and Suga (2006) and references therein.

Mode Water	Temperature	Salinity	Density
Name	**Range (°C)**	**Range (g kg^{-1})**	Anomaly (σ_0) (kg m^{-3})
NPTW	20.0–24.0	34.9–35.5	23.6–25.1
ESTMW	16.0–22.0	34.6–35.4	23.9–26.1
STMW	15.4–19.7	34.6–35.0	24.5–25.9
L-CMW	12.0–14.5	34.3–34.6	25.5–26.3
D-CMW	6.0–10.0	33.7–34.2	25.9–26.9
TRMW	4.0–9.0	33.0–34.0	26.3–26.6

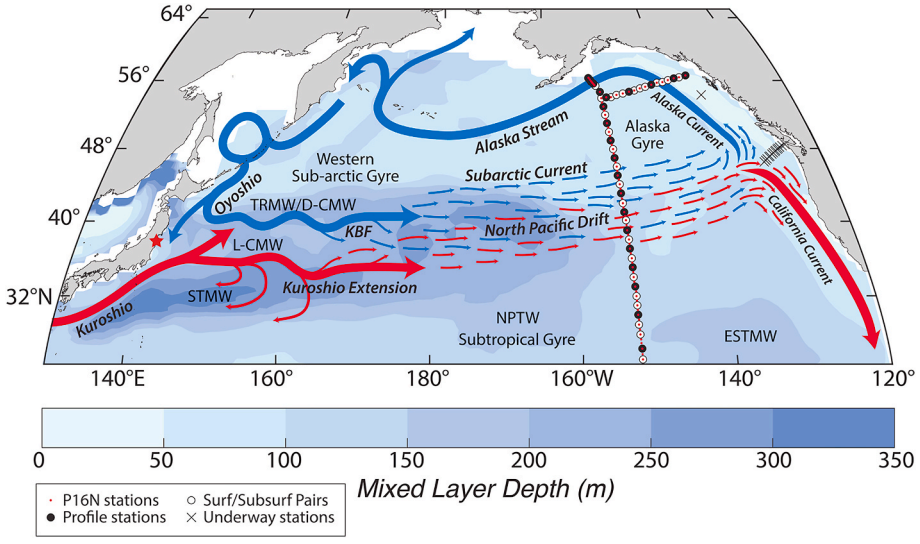

Fig. 1. Schematic of North Pacific circulation overlaid on mean March mixed layer depth (blue shading, from GODAS, 2015; units: m) for the period 2011–2015. Line thickness does not represent current strength. Major currents, gyres and specific waters mass formation regions mentioned in the text are labeled: Kuroshio Bifurcation Front (KBF), Subtropical Mode Water (STMW), Light Central Mode Water (L-CMW), Dense Central Mode Water (D-CMW), Transition Region Mode Water (TRMW), Eastern Subtropical Mode Water (ESTMW) and North Pacific Tropical Water (NPTW). Hydrographic station locations for the northern end of the 2015 P16N/leg 2 occupation are shown as red dots. Black symbols indicate the location of cesium samples: open circle = subsurface/surface pair, filled circle = profile, and cross = underway surface sample. All P16N cesium stations are shown in Fig. S1. The red star is FDNPP location. (For interpretation of the references to color in this figure legend, the reader is referred to the Web version of this article.)

2004).

North Pacific Tropical Water (NPTW $23.6 < \sigma_0 < 25.1$), which is formed to the south of 30°N in the saline surface water Ekman convergence at the center of the subtropical gyre between 15° and 25°N, 160°E-120°W (Katsura et al., 2013) is also of interest because its 30°N limit may impact the farfield distribution of Cs_F. While warmer and saltier than North Pacific MW, it partially overlaps ESTMW and STMW geographically as well as in density space.

A number of MW characteristic definitions exist in the literature (e.g. Hautala and Roemmich, 1998; Mecking and Warner, 2001; Oka and Suga, 2005; Qu et al., 2001; Oka et al., 2007, 2011; 2015; Rainville et al., 2014; Katsura, 2018) some of which suggest narrower or slightly offset ranges. We use those described in Table 1. Across the broader Pacific, these waters have been recognized by their natural physical characteristics obtained at the time of formation. Here, we have the opportunity to use an anthropogenic tracer (i.e. Cs_F) that was unintentionally introduced to the ocean at a time and location that coincided with water mass formation.

1.2. Radiocesium in the Pacific

History of Ocean Cs prior to FDNPP Release: The largest input of cesium isotopes to the ocean is fallout from atmospheric nuclear weapons testing in the late 1950s and early 1960s, which was highest in mid-latitudes in the northern hemisphere (e.g. Aarkrog, 2003). Programs in the 1960s and 1970s began to measure the weapon's testing Cs (Cs_{WT}) oceanic distribution along with several other isotopes (e.g. tritium, ^{14}C, ^{90}Sr, and Pu). Its soluble nature (e.g. <0.1% of Cs is caught on a one-micron filter; Buesseler et al., 2012) allows Cs to be used as an ocean circulation tracer.

Additional ^{137}Cs inputs to the ocean from reprocessing plants in Europe peaked in the 1970s, but did not impact Pacific waters. In 1986, Chernobyl became the largest accidental release of ^{137}Cs. Although the total atmospheric release of radioisotopes from Chernobyl was about ten times that of FDNPP (Steinhauser et al., 2014), only a small fraction was deposited in the North Pacific. Therefore, the 15–20 PBq (e.g. Inomata et al., 2018; Aoyama et al., 2019) of input via atmosphere and ocean from the 2011 FDNPP accident represents the largest accidental source of radioisotopes to this basin. It increased the existing 2011 North Pacific Cs inventory of 69 PBq (Aoyama et al., 2012) by 20–27% (Inomata et al., 2016; Aoyama et al., 2016b, 2019).

With its short half-life, ^{134}Cs uniquely "tags" water as being of Fukushima origin (i.e. Cs_F). The longer half-life of the ^{137}Cs isotope means that the ^{137}Cs signal that entered the surface ocean during nuclear weapons testing prior to the treaty signed in 1963 is still measurable today (Bowen et al., 1980; United Nations, 2000). More than half a century of ocean mixing and dispersion has lowered the concentrations of this weapons-based isotope (Cs_{WT}) to background levels of 1.0–2.0 Bq m^{-3} (Aoyama and Hirose, 2008; Inomata et al., 2009; Aoyama et al., 2012). Due to the lack of deep water formation fallout delivery to the surface Pacific Ocean has tended to remain in the upper water column. How deeply the ^{137}Cs has been mixed down over the last half century in the eastern North Pacific and the effects of this mixing on the uniformity of the Cs_{WT} background in the region will be discussed in Section 3.3.

FDNPP Radionuclide Release: The FDNPP, which includes six reactors, is located just north of the Kuroshio separation point on the northeast coast of Japan (37°25′N, 142°2′E, Fig. 1). In March 2011, the offshore earthquake, and resulting tsunami and aftershocks caused a loss of power at the FDNPP. Soon thereafter, destabilization led to both a release of radioactive materials to the atmosphere (i.e. widespread atmospheric deposition – AD) through venting, hydrogen explosions and fire, and a leakage of coolant water through direct discharge into the ocean, i.e., the point-source direct ocean discharge – DOD – just off the FDNPP (Chino et al., 2011; Butler, 2011; NSCJ, 2011; Buesseler et al., 2017). Both AD and DOD had a $^{134}Cs/^{137}Cs$ ratio of 0.99 ± 0.03 (Buesseler et al., 2011). While no direct fallout observations over the oceans exist and total magnitudes are still subject to debate, transport models suggest that the bulk of the AD to the ocean occurred to the northeast of the plant (e.g. Stohl et al., 2012; Tsubono et al., 2016; Aoyama et al., 2016b) and that about three-quarters of the contamination that entered the atmosphere landed in the Northwest Pacific in near-shore waters (Buesseler et al., 2017; Inomata et al., 2018).

Injected from the shoreline, at its peak on April 6, 2011, the highest Cs activities measured in the ocean off the FDNPP were order 68×10^6 Bq m^{-3} (Buesseler et al., 2017 and others), representing more than a 10 million-fold increase over prior activities. Both observational evidence and numerical model simulations indicate relatively rapid (within a few months) advection of contaminants eastward (Buesseler et al., 2012; Tsumune et al., 2017 Rypina et al., 2013) into the highly energetic mixed water region in the confluence of the Kuroshio and Oyashio (Fig. 1). Cs levels decreased rapidly in the months following the accident as maxima mixed vigorously and moved offshore carried by the strong and highly turbulent Kuroshio Current and KE (Rossi et al., 2013). Although, 90% of the DOD occurred by 12 April 2011, attesting to continued leakage, ocean Cs levels close to the FDNPP remained elevated – 1000 Bq m^{-3} (outflow ≈ 10 GBq day^{-1}) four years after the accident (Buesseler et al., 2011, 2017) and 20 Bq m^{-3} (outflow ≈ 2 GBq day^{-1}) seven years after (Kyodo News, 2018).

1.3. Ocean focused investigations of FDNPP radionuclides

In 2011, the Japanese government (MEXT, 2011) and the Tokyo Electric Power Company (TEPCO, 2011) monitored direct ocean discharge within 30 km of the coast. Near shore monitoring (to within 1 km of the power plant) continues to today (TEPCO, 2017; Kyodo News, 2018). Repeat surveys have been undertaken in the western basin near Japan (e.g. Men et al., 2015; Kumamoto et al., 2014, 2017), but observations of the radionuclide activity in the open-ocean have been sporadic as opportunities have arisen. These observations include samples scattered across the basin (e.g. Aoyama et al., 2011, 2012, 2013, 2016a, b, 2019; Kameník et al., 2013), and more recent samples obtained as ancillary measurements on transects (e.g. Yoshida et al., 2015; Kaeriyama et al., 2016;Kumamoto et al., 2016) and in the eastern basin (Smith et al., 2015, 2017), as well as samples provided by both members of the science community and the public along the U.S./Canadian shoreline (ORO, 2013). Surface drifters deployed near the FDNPP in early summer 2011 showed trajectories crossing the basin generally following the large-scale ocean circulation after one year (Rypina et al., 2013). From June 2011 observations it was determined that long-lived isolated eddies and western boundary current dynamics were the dominant factors defining Cs_F dispersion in the far western North Pacific on a 3-month time-scale (Rypina et al., 2013). As the contaminated water spread horizontally across the North Pacific basin, the modeling studies of Behrens et al. (2012) and Rossi et al. (2013) were among the first to report substantial vertical intrusion of Cs into the ocean interior, especially when the surface plume met late-winter/spring deep pycnostads in well-known MW formation regions.

Four meridional sections at 147°E (30 Oct. 2012–Nov. 5, 2012), 149°E (20 Dec. 2011–Feb. 9, 2012), 155°E (25 Oct. 2012–Oct. 29, 2012) and 165°E (10 Jun. - Jul. 16, 2012) provided early observational evidence of entrainment, subduction and advection of ^{134}Cs in MW to the north and south of the Kuroshio. About 9-months after the accident, observations at 149°E suggested that the bulk of the ^{134}Cs passed through the transition region (35°-40°N) between the surface and 200 m ($\sigma_\theta = 26.4$–26.8, maximum ~16 Bq m^{-3}) (Kumamoto et al., 2014). By the fall of 2012, at 147°E the signal remaining in the transition region was concentrated at 38°-40°N ($\sigma_\theta = 26.1$–26.4, maximum ~14 Bq m^{-3}) at 150 m (Kaeriyama et al., 2016, values decay corrected to Apr 6, 2011). At 155°E, the transition region signal had a similar maximum (~15 Bq m^{-3} at 38.5°N, $\sigma_\theta = 26.6$), but also a recognizable 100–300 core across from 34 N° to 40°N. At 36°-38°N there were secondary maxima (~14 Bq m^{-3}) at 400 m, $\sigma_\theta = 26.4$ that extended down to 500 m (Kaeriyama et al.,

2016).

These meridional lines also saw the subduction, capping and spreading of STMW to the south of the KE. In January–February 2012, a subsurface ^{134}Cs maximum (~18 Bq m^{-3} at 400 m) at 149°E, 34°N was observed and this 300–400 m core, although attenuating southward, was detectable as far south as 20°N (Kumamoto et al., 2014). By the fall of 2012, the ^{134}Cs core was observed at 200–400 m at 147°E, throughout the 30°-35°N region with maxima 10–14 Bq m^{-3} in the 24.6 to 26.1σ_θ range (Kaeriyama et al., 2016). These observations are consistent with those made a few months earlier at 165°E, which presented double ^{134}Cs cores to the south and north of the KE (at ~30°N/150 m and ~40°N/300 m, respectively) in a pattern of detectable signal that spread from ~23 to 46°N (Aoyama et al, 2016a).

Yoshida et al. (2015) investigated the spread of Cs_F on a 2-year timescale utilizing the samples obtained from the variety of cruises including the 2013 P02 transect that crossed the basin at 30°N. They found that at this latitude the leading edge of the surface Cs_F signal had reached 174°W by the spring of 2012. A year later, with an average advection speed of 5 cm s^{-1} it was observed at 160.6°W. This rate of spread at 30°N agreed well with drifter and model estimates (Aoyama et al., 2016a). Although the 30°N subsurface data set was sparse, it was found that two years after the accident the maximum Cs_F signal west of 173.3°E lay at ~300 m, but shoaled sharply to 200 m near the dateline and remained subsurface until the signal disappeared at 160.6°W.

At 40°N, Cs_F had reached the dateline by July 2012 suggesting an average advection speed of 8.5 cm s^{-1}, which slowed to ~5 cm s^{-1} by the time the signal reached 160° to 170°W (Yoshida et al., 2015; Inomata et al., 2018). In the northeast, Cs levels were being monitored along Line-P (Fig. S1). Here, Smith et al. (2015) first detected ^{137}Cs greater than the background (which they took to be ~1 Bq m^{-3}) ~1500 km west of the Canadian coast in June 2012. A year later, order 1 Bq m^{-3} values were observed on the Canadian Shelf and by early 2014, ^{137}Cs values as high as 2 Bq m^{-3} were observed throughout Line-P (Smith et al., 2017). These results were corroborated by 2014 observations obtained between Dutch Harbor, AK and Eureka, WA, where a clear FDNPP surface signal with ^{134}Cs values of 2–4 Bq m^{-3} was found in the Alaska Gyre along with one higher value (^{134}Cs = 5.4 Bq m^{-3}) off the coast WA (Yoshida et al., 2015).

Compiled surface ^{137}Cs measurements obtained between July 2011 and December 2012 across a broad expanse of the North Pacific Ocean (Aoyama et al., 2016a) suggest that in the Northeast Pacific, after the first few months, the effects of Fukushima sourced AD could not be distinguished from the weapons testing background. This result is supported by the findings of Buesseler et al. (2017) in their compilation of surface data ^{137}Cs that extends to April 2016 (see their figure 2) and Kumamoto et al. (2016) who concluded that the main bulk of the AD occurred in the Bering Sea and between 25°N and 50°N in the northwestern basin. So, while there was certainly some atmospheric delivery of Cs_F to the Northeast Pacific, the early lack of substantially elevated ^{134}Cs in the surface ocean to the east of the dateline suggests that Cs_F found at 152°W in the spring of 2015, whether AD or DOD, was input to the ocean in the west and advected eastward. As the ^{134}Cs/^{137}Cs ratio in the AD and DOD were the same, the two are indistinguishable in our Cs data set. Therefore, we presume that the ^{134}Cs signal observed in 2015 at 152°W is derived from a combination of the FDNPP DOD and AD that entered the ocean in the western basin. Likewise, we assume that patterns of ^{137}Cs that mimic those of ^{134}Cs are from an FDNPP source (we will come back to this in Section 3.3).

Here, we present the 2015 distribution of Cs_F in the Northeast Pacific along 152°W. Using these observations, we seek to elucidate the history of mode waters that have traversed the basin over the previous 4 years.

2. The 2015 radionuclide dataset, chemical analysis and distribution

2.1. Sampling

In the spring of 2015 (Table 2) 395 radionuclide samples were obtained from the GO-SHIP occupation of the 152°W line P16N (Fig. 1and S1) beginning with twenty 12-sample radionuclide-only casts each going from ~10 m to ~1000 m. Use of the underway seawater system on station and efficient use of water remaining in the bottles after all other sampling had been completed on regular hydrographic casts produced another 155 samples.

These included surface samples obtained from the underway seawater system as the ship steamed from the outer boundary of the U.S. Exclusive Economic Zone (EEZ) into Seattle, a few short profiles in shallower waters coming up the slope toward Kodiak and Sitka, and about 50 surface/subsurface pairs. This sampling scheme provided ~1° spacing along 152°W and a more broadly spaced survey across the Alaska Gyre (Fig. 1and S1). The 'cross-gyre' transect began at 54.1°N, 151.1°W, 100 km east of the meridional line and with an average latitude of 55.5°N followed a portion of the 1993 WOCE P17N survey track. Of the 395 samples taken, 292 were on the 152°W line, 86 were on the cross-gyre transect, 15 were underway samples in the U.S. EEZ, and 2 were lost due to technical difficulties reducing the final number to 393.

2.2. Chemical analysis

Here we present results from three radioisotopes: ^{134}Cs, ^{137}Cs, and briefly ^{90}Sr (half-life = 28.90 yeas). Approximately 20 L seawater samples were collected into cubitainers for ^{137}Cs, ^{134}Cs and ^{90}Sr analyses. The samples were analyzed onshore at the Buesseler Laboratory at Woods Hole Oceanographic Institution using an ion-exchange resin-based method– potassium-nickel hexacyanoferrate (II) (KNiFC-Pan) (Šebasta, 1997; Breier et al., 2016) for γ-counting on high-purity germanium well-type detectors for an average counting time of 50 h.

Measurement errors include propagated recovery error (average 2.0 ± 0.0%) and detector count error (varies by sample). The average recovery was 98.5% ± 1.7% with a range of 81%–100% and a median 99.0%. Decay correction ^{134}Cs (^{137}Cs) measurement error ranged from 0.02 to 1.30 (0.01–0.60) Bq m^{-3}. Determined at the time of measurement, the average detection limits for both ^{134}Cs and ^{137}Cs are 0.1 Bq m^{-3} for Buesseler Laboratory measurements (Pike et al., 2012) and 0.03 Bq m^{-3} for the few low count samples that were sent to the HADES Laboratory (HADES, 2020). For example, the deep 650 dbar ^{134}Cs at 35°N (0.04 ± 0.02 Bq m^{-3}) was measured underground at HADES. Of samples sent to the underground lab, WHOI (HADES) found detectable ^{137}Cs in 43 (71) and detectable ^{134}Cs in 1 (25). No samples south of 30°N were measured at HADES. Henceforth, the term *significant* implies that a measurement is both greater than the detection limit and the estimated decay-corrected measurement error.

Samples were analyzed for ^{90}Sr in the Buesseler Laboratory via beta counting of its daughter product ^{90}Y (half-life = 64.1 h) by a method

Table 2
Start and end times and locations of the 2015 P16N radiocesium sampling.

Component	Start Location	End Location	Month/ Day Start	Month/Day End
Leg 1	3.1°N, 152.0°W	21.5°N, 152.0°W	4/29/ 2015	5/11/2015
Leg 2	22.5°N, 152.0°W	56.4°N, 152.0°W	5/27/ 2015	6/18/2015
Cross-Gyre	54.1°N, 151.1°W	56.8°N, 136.0°W	6/19/ 2015	6/23/2015
Underway	54.3°N, 134.9°W	48.5°N, 124.8°W	6/24/ 2015	6/27/2015

adapted from Tazoe et al. (2017). Fe hydroxide co-precipitated samples were filtered through a 25 mm QMA filter, dried, and fixed onto beta mounts that were counted on Risø beta detectors (Risø National Lab; Roskilde, Denmark). The detection limit ranged from 0.2 to 0.4 Bq·m^{-3} for an approximately 90 h counting time. Aliquots were taken before and after adsorption for stable ^{137}Cs, ^{134}Cs, ^{90}Sr, and ^{90}Y to determine extraction recovery via inductively coupled plasma mass spectrometer (Thermo iCAP Qc). All results reported here, unless otherwise noted, are based on concentration decay corrected to the major liquid discharge event date of April 6, 2011 (Buesseler et al., 2011). All sampling locations and the associated Cs activities have been submitted to the US Global Ocean Carbon and Repeat Hydrography Program (CCHDO, 2019) and the IAEA MARIS database (MARIS, 2019).

2.3. The 2015 Northeast Pacific radionuclide distribution

On P16N, Cs_F is evident from 30°N to the coast of Alaska (Fig. 2). Of the 393 Cs samples, 123 (31%) have significant ^{134}Cs activities (i.e. above the detection limit and greater than their measurement error). As expected, due to the existence of the Cs_{WT} background, a larger number 372 (95%) have significant ^{137}Cs. Of the 82 surface ^{134}Cs samples (Fig. 2a), 37 (45%) have significant activities. There are marked southern and northern boundaries to the surface signal at 30°N and 49°N. Significant subsurface activities are apparent on the approach up the northern slope (within the Alaska Stream) and scattered across the Alaska Gyre including in the path of the Alaska Current. We return to the cross-gyre leg in the next subsection and here focus on the 292 152°W samples.

Radiocesium distribution along the 152°W Meridian: Along 152°W with 106 (36%) of the ^{134}Cs samples having significant activities. 278 (95%) of the 152°W samples had significant ^{137}Cs signals (Fig. S2). Of the 186 samples with ^{134}Cs below the detection limit, 172 have detectable ^{137}Cs.

The minimum significant 152°W surface ^{134}Cs is 0.04 ± 0.02 Bq m^{-3}. The five largest surface values (>7.0 Bq m^{-3}) lie along 152°W between 41°N and 44°N. The next highest (6.1 ± 0.6 Bq m^{-3}) is longitudinally contiguous at 40°N. Deeper in the water column (Fig. 2b–f) the greatest activities are slightly more spread between about 39°N and 45°N. The highest ^{134}Cs activity (10.3 ± 0.8 Bq m^{-3}) is found at 50–100 dbar at 43°N (Fig. 2c). At 30°N all ^{134}Cs values are≥1 Bq m^{-3}. The southernmost significant ^{134}Cs measurement, which is also subsurface (140 dbar), appears as an outlier (0.4 ± 0.1 Bq m^{-3}) above the detection limit at 20°N as no other is found south of 30°N at any depth (Fig. 2). Not so for ^{137}Cs. Detectable ^{137}Cs (Fig. S2) is found throughout the section from the southernmost profile at 3°N to the Alaska Shelf. The only break is between 12° and 22°N where there are no samples in the shallowest bin. The southern boundary of the ^{134}Cs signal tends northward with depth, a pattern made clearer by a latitude/pressure section plot (Fig. 3). North of ~36°N, both the maximum value in each profile and the deepest detectable signals shoal to the north. The Cs_F follows the shoaling of the isopycnals northward. The abrupt boundary at 30°N is clear in the ^{134}Cs sections.

The ^{137}Cs signal confirms the ^{134}Cs findings (Fig. 3b, d) with maximum activities in similar geographic, depth and density spaces. Note, that although the signal is weak, the southern boundary is less abrupt giving the impression that the measurement at 20°N (that appeared as an outlier in the ^{134}Cs distribution) is the southernmost extension of the deepest signal shoaling to the south. Whether or not this signal is following isopycnals will be discussed in the analysis of the circulation and local Cs_{WT} background (Section 3.3).

A^{134}Cs section (Fig. 3a, c) highlights the subsurface and compact nature of Cs_F at 152°W. The two largest activities, those greater than 10 Bq m^{-3}, are both found at 43°N. The 10 largest values are confined between 25.2 and 26.5σ_0, all MW densities. Even the outlier at 20°N and the deepest detectable signal (at 645 dbar) still lie with MW density bounds as defined in Table 1.

Radiocesium distribution on the zonal transect crossing the Alaska Gyre: As noted earlier, some low, but significant, ^{134}Cs values were observed across the gyre (Fig. 2). At first glance the mainly surface signal seems best described as spots of activity; in the east, interior to the slope approaching Sitka, in the west near 152°W, and in the center of the gyre. The latter two and especially the central gyre signal reached deeper into the water column, but still only to ~140 dbar (Fig. 2c and d). As on the meridional line, the maximum ^{134}Cs activity (2.5 ± 0.4 Bq m^{-3}) lies subsurface (80 dbar at 138.3°W, 56.4°N). The section plot (Fig. 4a) provides some further insight as it suggests that the ^{134}Cs signal is mainly located above the pycnocline. The exception is the profile taken in the steeply sloping isopycnals at 149°W where ^{134}Cs has been

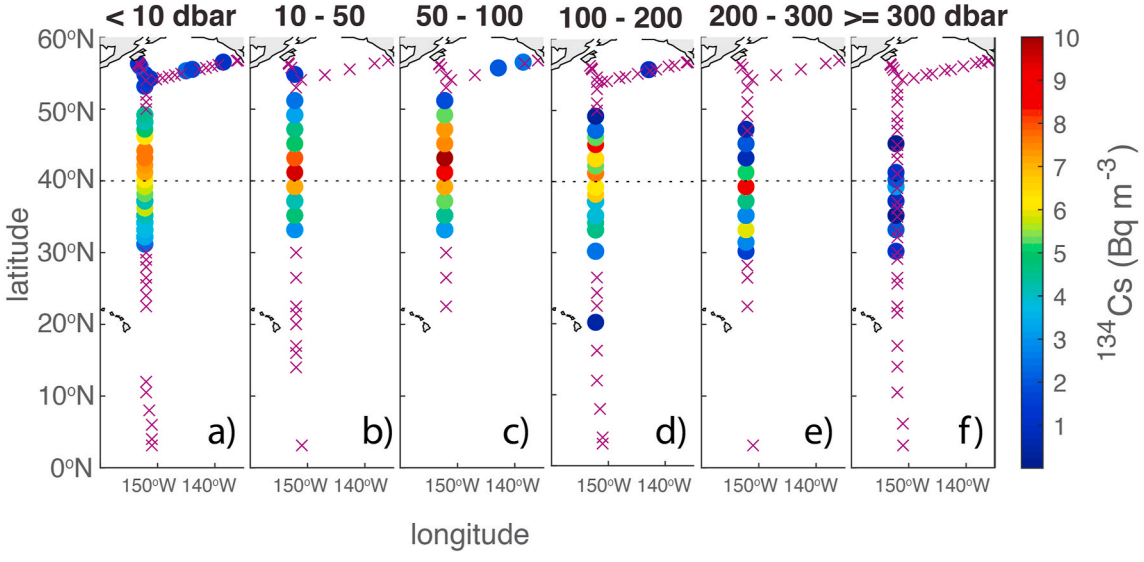

Fig. 2. Geographic distribution of detectable P16N^{134}Cs in pressure bins, shallow/left to deep/right: a) 0–10 dbar; b) 10–50 dbar; c) 50–100 dbar; d) 100–200 dbar; e) 200–300 dbar; and f) below 300 dbar. Upper surface pressure boundaries are inclusive. Colors indicate magnitude of activity decay corrected to April 6, 2011. Color bar is saturated at 10 Bq m^{-3}. Higher activities are plotted over lower activities, so be aware that deeper samples may overlay shallower samples. Values below the detection limit are shown by 'x' (see text). Fig. S2 is the equivalent for ^{137}Cs. (For interpretation of the references to color in this figure legend, the reader is referred to the Web version of this article.)

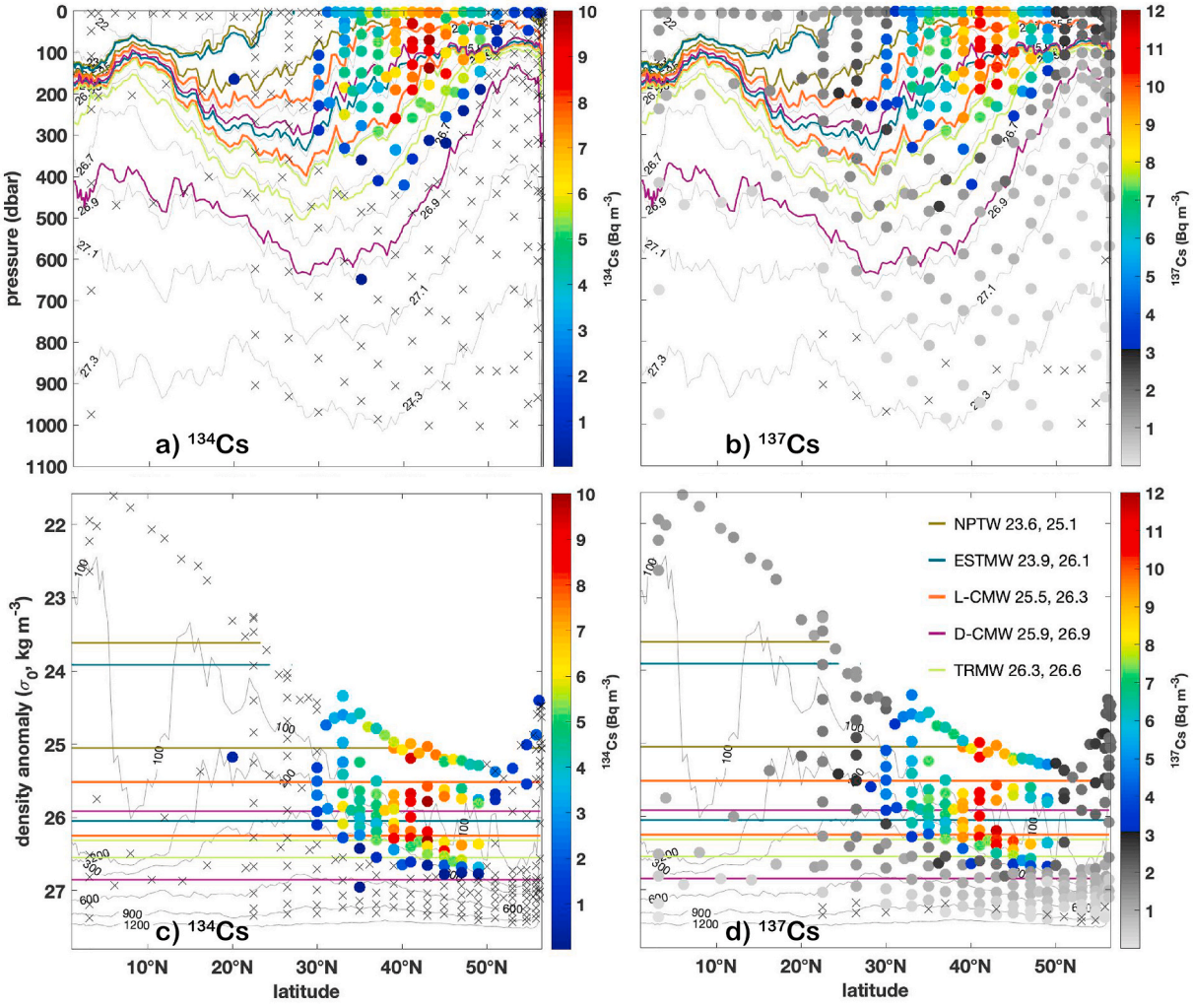

Fig. 3. a) ^{134}Cs along 152°W in latitude-pressure space. Colors indicate magnitude of activity decay corrected to April 6, 2011. Color bar is saturated at 10 Bq m^{-3}. Gray x symbols are values below detection limit; gray lines are potential density anomaly relative to 0 dbar; colored lines are boundaries for each Table 1 water mass according to the legend in (d); b) Same as (a) for ^{137}Cs. Color bar saturated at 12 Bq m^{-3}; c) same as (a) in latitude-σ_0 space with gray curves representing pressure contours; d) Same as (c) for ^{137}Cs. Note, ^{137}Cs gray scale below 3 Bq m^{-3}. This value has been chosen to facilitate comparison to the ^{134}Cs figure and to improve the representation of weaker signals. Although it is representative of the maximum remaining Cs_{WT} in the region, it should not be taken as a hard and fast estimate as Cs_{WT} has a latitudinal dependence (see Section 3.3). (For interpretation of the references to color in this figure legend, the reader is referred to the Web version of this article.)

subducted locally in the front or has arrived at this location in the denser waters (e.g. perhaps TRMWs/D-CMWs outlined by light green/purple contours) of the boundary current. Whichever the case, Cs_F is being advected around the gyre in the boundary current which, according to both the density field in Fig. 4 and the P16N Lowered Acoustic Doppler Current Profiler (LADCP) direct velocity measurements is lying offshore of the easternmost stations.

The ^{137}Cs cross-gyre maximum (3.8 ± 0.2 Bq m^{-3} found at the surface at 144.8°W, 55.2°N) was not co-located with the ^{134}Cs maximum (which had an associated ^{137}Cs of 3.1 Bq m^{-3}). Nevertheless, the pattern of ^{137}Cs (Fig. 4b) is similar and fills in some of the gaps left by the ^{134}Cs measurements in the near surface. All ^{137}Cs with activity greater than the canonical background of 1–2 Bq m^{-3} were found shallower than the upper boundary of L-CMW (25.5 σ_0, orange curve). Note also that Fig. 4 only shows the samples going down to 300 dbar. The deepest detectable cross-gyre ^{137}Cs was found at 1000 dbar at the longitude of the deepest ^{134}Cs value (142.5°W, Fig. S3). However, ^{137}Cs was not detected everywhere along the gyre section below 500 dbar. To the west, toward 152°W and away from the central portion of the cross-gyre transect, the ^{137}Cs signal shoals. At the westernmost cross-gyre profile (151.1°W) the deepest ^{137}Cs signals lies at ~450 dbar, well above the deepest cross-gyre signals at 1000 dbar.

***Radiocesium distribution on underway leg into Seattle*:** As in the cross-gyre samples, the ^{134}Cs signal in the underway samples is not strong (<2.5 Bq m^{-3}), but is significant (Fig. 5). The observations indicate a stronger radionuclide signal associated with denser waters. The eastern boundary along the North American west coast is well known as an upwelling system and here we see that as surface waters become denser on the coastal approach, Cs_F traces the shoaling isopycnals where they outcrop. The ^{137}Cs observations (Fig. S4) support this result, though not quite as clearly as they are clouded by variable and upwelling Cs_{WT}. Just to the north (48.5°-50°N), Line-P (Fig. S1) density sections based on observations show shoaling isopycnals – supporting the idea of inshore upwelling within 500 km of the coast in this region and timeframe (see August 2015 panels of Smith et al. (2017) Fig. 2).

In summary, the P16N Cs sampling provides a May–June 2015 picture of Cs_F in the northeast Pacific with the deepest significant ^{134}Cs measurement at ~650 dbar; the ten highest values between 39°N and 45°N from just below the surface to 260 dbar; a maximum signal at 43°N (70 and 145 dbar); and an abrupt cutoff at 30°N. These observations in

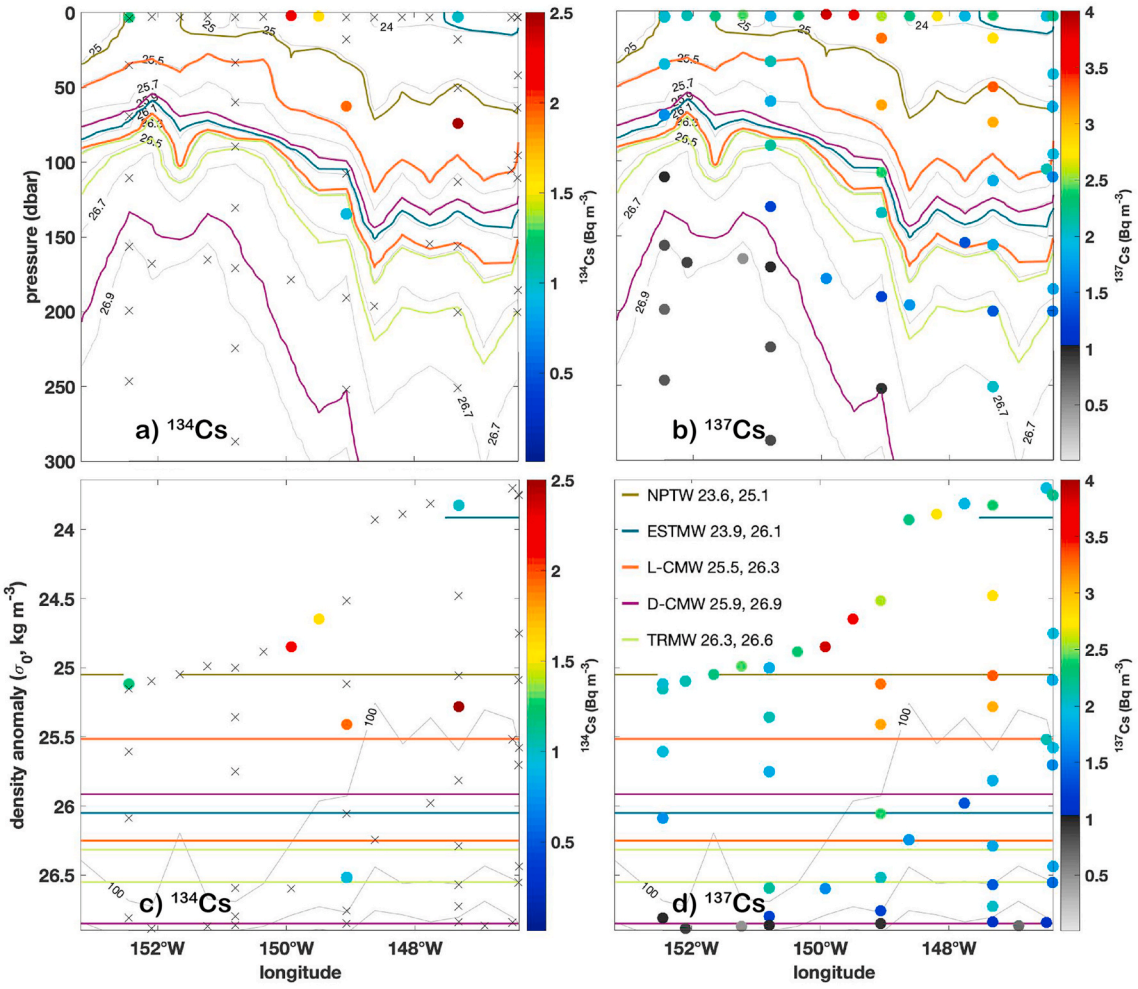

Fig. 4. a) Significant ^{134}Cs along the cross-gyre transect in longitude-pressure space. Colors indicate magnitude of activity decay corrected to April 6, 2011. Color bar is saturated at 2.5 Bq m^{-3}. Gray x symbols indicate values below detection limit; gray lines are potential density anomaly relative to 0 dbar; water mass density boundaries are indicated in color as in Fig. 4; b) Same as (a) for ^{137}Cs. Color bar saturated at 4.0 Bq m^{-3} and a change to gray scale occurs at 1 Bq m^{-3}. As for Fig. 3, gray scale does not represent C_{WT}, but is provided to improve the representation of weaker, but detectable ^{137}Cs signals; c) Same as (a) in longitude-σ_0 space with gray curves representing 100, 200 and 300 dbar; d) Same as (c) for ^{137}Cs. Note, that depths, densities and color bar are not the same as those in Fig. 3. Equivalent for ^{137}Cs down to 1000 dbar is provided in the supplementary material (Fig. S3). (For interpretation of the references to color in this figure legend, the reader is referred to the Web version of this article.)

the east are consistent with earlier findings in the west (e.g. Kumamoto et al., 2014; Kaeriyama et al., 2016) with a stronger signal subsurface in the MW densities. In the eastern basin there is a shoaling of Cs_F northward along 152°W with the MW, an indication of the transport of a weak surface signal around the Alaska Gyre in the boundary current, and a stronger subsurface signal away from the coast at ~55°N. The interior gyre presents a 1000 dbar deep bowl shaped ^{137}Cs signal with the deepest values shoaling toward the coast to the east and to ~450 m to the west at 152°W. Lastly, a pattern of upwelling Cs_F was found on the coastal approach into Seattle.

3. Discussion

The timing of maximum FDNPP AD and DOD introduced to the western North Pacific in late winter/early spring and the proximate North Pacific MW formation regions made it reasonable to assume from the beginning that Cs_F would find its way into MW. As discussed earlier, many studies both observation- and model-based have borne this assumption out (e.g. Rossi et al., 2013; Kumamoto et al., 2014, 2017; Yoshida et al., 2015; Kaeriyama et al., 2016; Aoyama et al., 2016a; Kumamoto et al., 2017; Smith et al., 2017). Updating Kaeriyama et al. (2014), Kaeriyama et al. (2016) estimate that by the fall of 2012, 4.2 ± 1.1 PBq Cs_F had penetrated STMWs, leading Inomata et al. (2018) to conclude that 2.5 ± 0.9 PBq Cs_F had been injected into CMWs. While only 22% of the 152°W water column can be characterized as one or more of the MW according to all three Table 1 characteristics (Θ, S, and σ_0) nearly 75% have potential densities in MW ranges, so we take the opportunity to determine the relative distribution and their water column Cs_F inventory.

3.1. The source of mode waters found at 152° W

The L-CMW formation region lies directly in the path of the DOD between the fronts to the north and south (Fig. 1). However, in Θ/S space (Fig. 6), while one of ten largest observed ^{134}Cs activities (largest dots circled in black) is associated with L-CMW densities, nine of these ten as well as the deepest signals are associated with D-CMW, and in particular a regime where D-CMW characteristics overlap those of TRMW. Kumamoto et al. (2014) and Kaeriyama et al. (2016) reported that between 147° and 155°E most of signal found in the 2012 transition region (35°-40°N) was in "CMW", but more precisely it was found in waters with TRMW/D-CMW densities.

MW in 2015 at 152° W and 2011–2015 MW Formation: To explain why we see Cs_F so clearly in D-CMW and TRMW at 152°W, but far less so

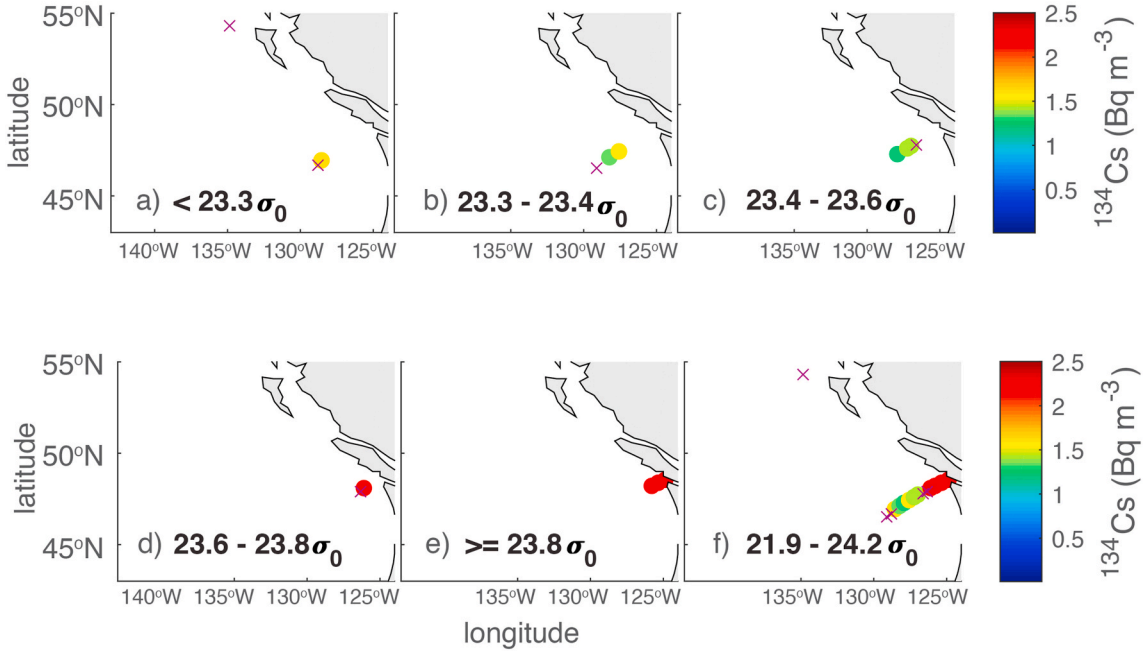

Fig. 5. Surface ^{134}Cs from underway samples in density anomaly bins. Densities are calculated from the ship's underway seawater system temperature and salinity sensor data (see explanation in the text). a) Density less than 23.3 σ_0; b) 23.3–23.4 σ_0; c) 23.4–23.6 σ_0; d) 23.6–23.8 σ_0; e) greater than 23.8 σ_0; and f) the full range 21.9–24.2 σ_0. Upper surface density boundaries are inclusive. Colors indicate magnitude of activity decay corrected to April 6, 2011. Color bar is saturated at 2.5 Bq m^{-3}. Magenta x symbols indicate values less than the detection limit of 0.1 Bq m^{-3}. Equivalent figure for ^{137}Cs is provided as Supplementary Fig. S4. Equivalent figures in pressure space are not shown as these all surface measurements. (For interpretation of the references to color in this figure legend, the reader is referred to the Web version of this article.)

in L-CMW and STMW, we follow the work of Bingham and Suga (2006, henceforth BS06) to determine where and when these waters formed over the 2011–2015 timeframe and how they have been distributed since. BS06 compared the extent of MW formation regions in 2006 based on Argo float data to the climatological average formation regions suggested by the World Ocean Atlas 2001 historical hydrography (Conkright et al., 2002). They reported that the overall distribution of suggested STMW formation sites in that single year were similar to the climatological distribution. They also found that the denser CMW formation regions were quite patchy and limited in 2006, and concluded that they varied more spatially and temporally than those of STMW. BS06 did not look at TRMW because it was not defined as a distinct MW until the following year (Saito et al., 2007, 2011).

Here, we employ some 113 thousand 2011–2015 Argo float profiles (Argo, 2019) to identify both the formations sites and subsurface extent of North Pacific MW since the FDNPP accident. Following BS06, we used the winter (January–March) MW properties at 10 dbar to identify possible formation regions between 2011 and 2015 (Fig. 7, dark blue dots), noting that these can also represent outcrops. We interpret locations with MW properties at 100 dbar but not at the surface (Fig. 7, light blue dots) as capped MW formed at some recent point in time, not necessarily 2011–2015, and locations where those properties exist at both 10 dbar and 100 dbar (Fig. 7, pink dots) as 2011–2015 MW formation.

The distribution of the Argo database MLDs (Fig. S6, based on Holte et al. (2017)) generally agrees with the combined distribution from all our Fig. 7 panels. However, it is not possible to create a one to one comparison. For example, due to the deeper STMW, CMW and TRMW formation region MLDs, NPTW formation is washed out in the Fig. S6 representation, as is the westward extension of ESTMW formation (see Katsura (2018), his figure 7).

Focusing on the areas with MW properties in the upper water column during January–March timeframe between 2011 and 2015 (Fig. 7 pink dots), it can be seen that while the north/south extent of ESTMW (Fig. 7b) at the dateline was similar (27°-34°N), in 2011–2015 STMW formed in a narrower band (27°-37°N) than in either 2006 or the climatological past (20°-37°N) (See BS06 their figure 3). This difference highlights the large inter-annual variability in geographical delimitation and spatial extent exhibited by these MW formation regions. While such variability might be studied by treating the Argo database year-by-year, observational gaps hinder such analysis. In addition, our main period of interest (2011–2015) is temporally and spatially well represented by Argo, which give us confidence in our results. We therefore leave investigation of inter-annual variability to future research.

The combination of multiple years of data, averages out inter-annual variability, returning less patchy CMW formation sites (Fig. 7c and d) than the 2006 data alone. The patterns suggest the Cs_F could well have been mixed/remixed into different MWs in different years as it was advected through the various mid-basin formation regions. L-CMW has a geographical extent similar to the climatology while D-CMW extends further south in the far west (~37°-44°N for 2011–2015 compared to 40°-44°N for the climatology), suggesting D-CMW formation directly off the coast from the FDNPP during the 4 years of interest. The model-based results of Cedarholm et al. (2019) support this suggestion, reporting that the densest varieties of MW (as dense as 26.8σ_Θ) were formed in 2011 in the transition region. TRMW formation sites (Fig. 7a) during the more recent time frame are limited to a relatively thin line (40°-43°N) west of 170°E. To the south, possible NPTW formation sites span most of the basin, expanding in latitude toward the east, but remaining to the south of 30°N. This is consistent with the Nie et al. (2016) analysis of ECCO model output that determined that NPTW subducts within the 20°-30°N band along 150°E-130°W. Of all these suggested formation regions, only ESTMW and NPTW overlap with the 152°W line. They both do so to the south of 30°N, indicating MW found to the north would have to have been advected into the region.

While all MW formation regions in the western basin lie within close proximity of the FDNPP, the STMW region is blocked by the Kuroshio and KE fronts (e.g. Rypina et al., 2013). Nevertheless, results from the western basin suggest that Cs_F contaminated waters have been subducted across the front (e.g. Kumamoto et al., 2014; Garraffo et al.,

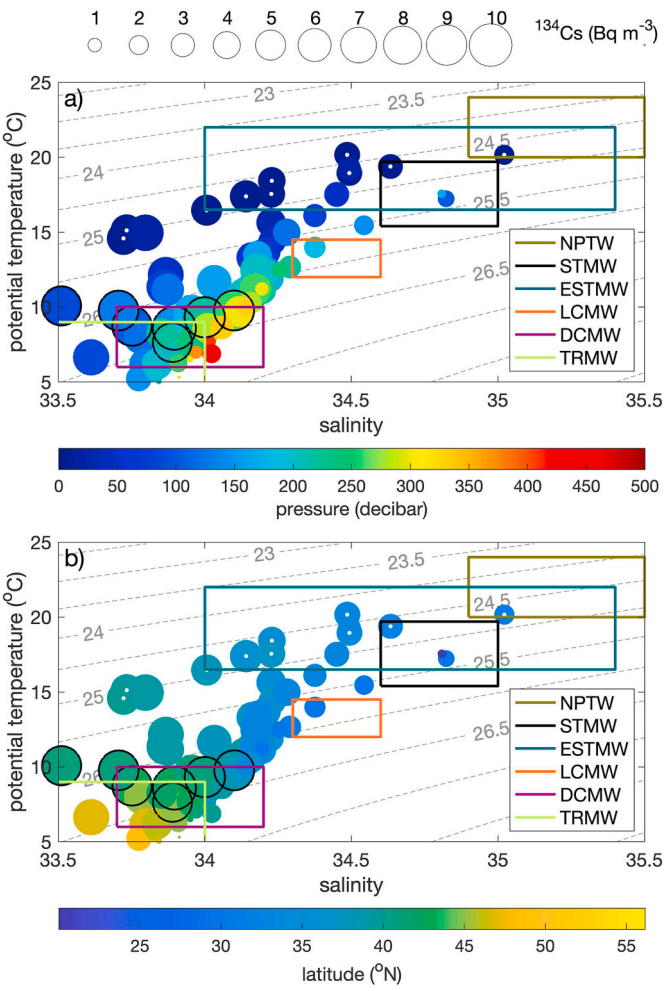

Fig. 6. Potential temperature/salinity distribution of waters associated with ^{134}Cs samples on the 152°W line. Size indicates magnitude of activity (scale provided at top of the figure). Surface (~5 m) samples have white dots in their centers. Ten largest values are outlined in black. Colored rectangles and contours outline the Θ/S and σ_0 space for each water mass as defined in Table 1, respectively. Colors match those used in Fig. 4. Circle colors indicate a) pressure and b) latitude associated with each sample. Equivalent figure for ^{137}Cs is provided as Supplementary Fig. S5. (For interpretation of the references to color in this figure legend, the reader is referred to the Web version of this article.)

2014; Yoshida et al., 2015; Aoyama et al., 2019). These waters have entered the recirculation where STMW forms (e.g. Aoyama et al., 2019). Such southward crossing, expected to occur more easily further out in the basin where the current becomes more diffusive (Rypina et al., 2014), has indeed occurred (e.g. Yoshida et al., 2015; Cedarholm et al., 2019).

Looking deeper in the water column (Fig. 8) provides insight into where the various MWs exist inside and outside their formation regions. All five of the water masses discussed overlap with the 152°W line at some location and depth in the subtropics or to the north (Figs. 7 and 8). From the surface to 100 dbar, NPTW exists well south of 30°N, and it recedes southward with depth (Fig. 8e): a pattern that suggests that what little Cs_F found to the south of 30°N may be associated with NPTW. It is, however, also true that ESTMW (Figs. 7b and 8b) water properties exist in the same region and with a much broader fingerprint at depth. Therefore, we are not in a position to say whether the few Cs_F observations found to the south of 30°N are the result of local mixing of AD or trans-basin advection.

MW in 2015 at 152°W and Circulation: The previous discussion explains why we might expect to see the strongest 152°W Cs_F signal in D-CMW/TRMW, but does not necessarily explain the weakness of the L-CMW signal (Fig. 6a). Upon exiting their respective formation regions, L-CMW and D-CMW/TRMW are both advected eastward in the anticyclonic subtropical gyre circulation. However, while the former does so predominantly on the southern (in)side of gyre, the latter takes the northern (out)side route. This suggests that L-CMW tagged with Cs_F may have turned southward and eastward before arriving at 152°W. This pattern is consistent with the observations of $^{137}Cs_{WT}$ in L-CMW in the subtropical gyre further east at 165°E (e.g. Aoyama et al., 2008, their figure 3). Note, that at depth, subducted L-CMW may reach the 152°W (Fig. 8c), but only to the south of 30°N where no Cs_F was found in 2015, i.e. timescales longer than 4-years may be necessary. Subsurface waters with D-CMW and TRMW properties extend to and beyond 152°W (Fig. 8a, d). At 400 dbar (Fig. 8, light blue dots), the pressure of our deepest non-outlying Cs_F signals (Fig. 3a), both TRMW and D-CMW cross 152°W; TRMW at and just south of 40°N and D-CMW in a broad region from ~43°N to 18°N.

At these pressures, TRMW and D-CMW properties are found in a sweeping curve around the subtropical gyre – a signal not seen in the 2015 Cs_F observations, which are limited by the 4-year timescale. A similar timescale (~3–5 years) is necessary for the core of the radionuclide plume to be simulated at about 500 m near 150°W/30°N (Rossi et al., 2013, see their figure 4 and Section 3.5). Water at both 200 dbar and 400 dbar (pink dots) at 152°W have D-CMW properties between about 39° and 43°N and so spans of our maximum Cs_F signal. At 200 dbar, D-CMW/TRMW properties overlap at ~45°N and extend around the boundary of the gyre in the Alaska Current, but only TRMW properties are seen further west in the Alaska Stream. They are also seen at 100 dbar in this boundary current (Fig. 7a light blue dots). Both patterns suggest that near Sitka, the measured Cs_F could be associated with upwelled versions of either of these water masses, but it is TRMW that has brought Cs_F fully around the Alaska Gyre to where it was measured off the Alaska Shelf near Kodiak. This process is consistent with Line-P findings (Smith et al., 2017) and the Rossi et al. (2013) modeling study.

3.2. 152°W radiocesium inventories

To obtain inventory estimates, water properties along 152°W were interpolated (but not extrapolated) onto a regular vertical (2 dbar) and meridional grid (0.05° latitude) using a natural nearest neighbor interpolation. Given the relative lack of deep observations, all inventory calculations were performed between 0 and 700 m (a depth chosen to include our deepest ^{134}Cs signal). Integrating vertically (Fig. 9a) the maximum water column inventories of both ^{137}Cs and ^{134}Cs are found at ~40°N (2.9×10^3 Bq m^{-2} and 1.9×10^3 Bq m^{-2} per meter of latitude, respectively). Integrating along 152°W and assuming a 1 m width, we find local along-line (3.0°-56.45°N) water column inventories of 8.3×10^9 Bq and 3.2×10^9 Bq for ^{137}Cs and ^{134}Cs, respectively. The difference between these two inventories (Fig. 9a, dotted line) is our first rough estimate of the shape of the Cs background at 152°W. To determine the fraction of the Cs_F inventory in each of the water masses present in the region, we define three additional waters masses so as to cover most of the water column above 700 m: (SSURF) surface water to the south of 30°N, defined as warmer, fresher and lighter than any in Table 1; (GASURF) Gulf of Alaska surface water defined to the north of 40°N and includes waters colder, fresher and lighter than those defined in Table 1; and (GAIW) Gulf of Alaska Intermediate Water, which spans a range of temperatures and salinities but in particular, is denser than 26.9 σ_0 (You et al, 2000; Kouketsu et al, 2007).

Quantifying what can already be generally seen in the pattern of isopycnal contours in Fig. 3 and 44% of the 152°W water column can be associated with waters whose potential temperature (θ), salinity (S) and potential density anomaly (σ_0) (rectangles in Fig. 6) lie in the range of one or more of the six water masses presented in Table 1 (plus SSURF, GASURF, and GAIW). If only density is used, 96% is captured, but there

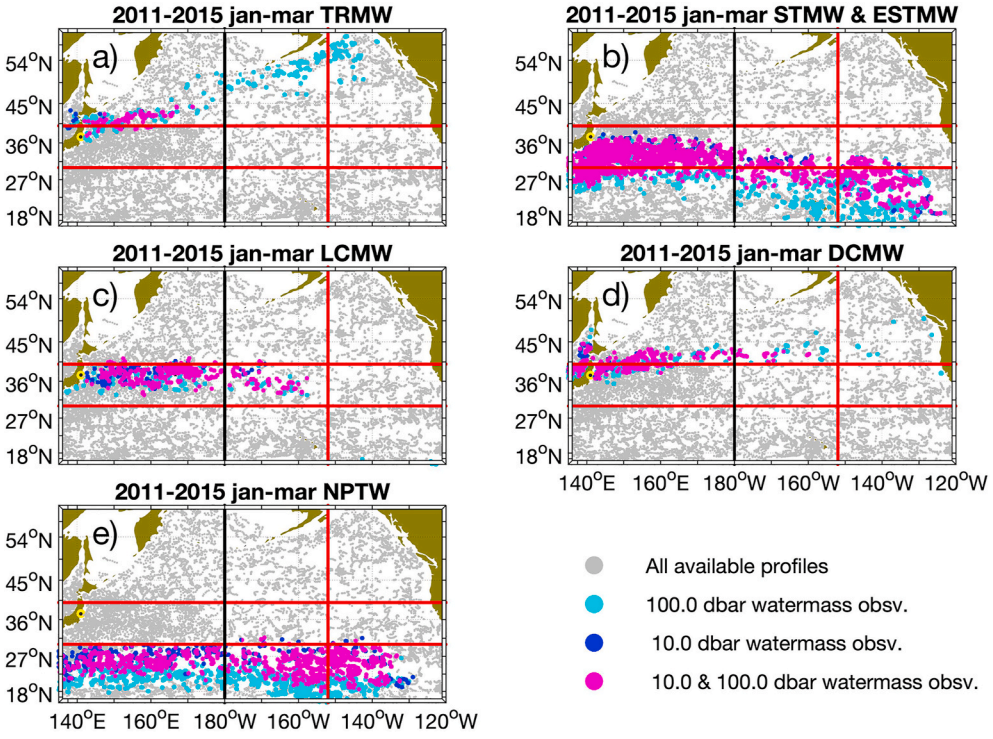

Fig. 7. Locations of Argo profiles for the months of January–March between March 2011 and June 2015 (gray dots). Profiles with the temperature, salinity and density characteristics of a) TRMW, b) STMW west of the dateline and ESTMW east of the dateline, c) L-CMW, d) D-CMW and e) NPTW at 10 dbar (dark blue dots, i.e. possible formation sites), at 100 dbar (light blue dots, i.e. capped subsurface sites), and at both 10 dbar and 100 dbar (pink dots, i.e. formation sites). Water mass definitions are provided in Table 1. For reference: black line at 180° longitude, red lines at 30°N, 40°N and 152°W. Yellow circle with black dot on Japan coast indicates FDNPP. (For interpretation of the references to color in this figure legend, the reader is referred to the Web version of this article.)

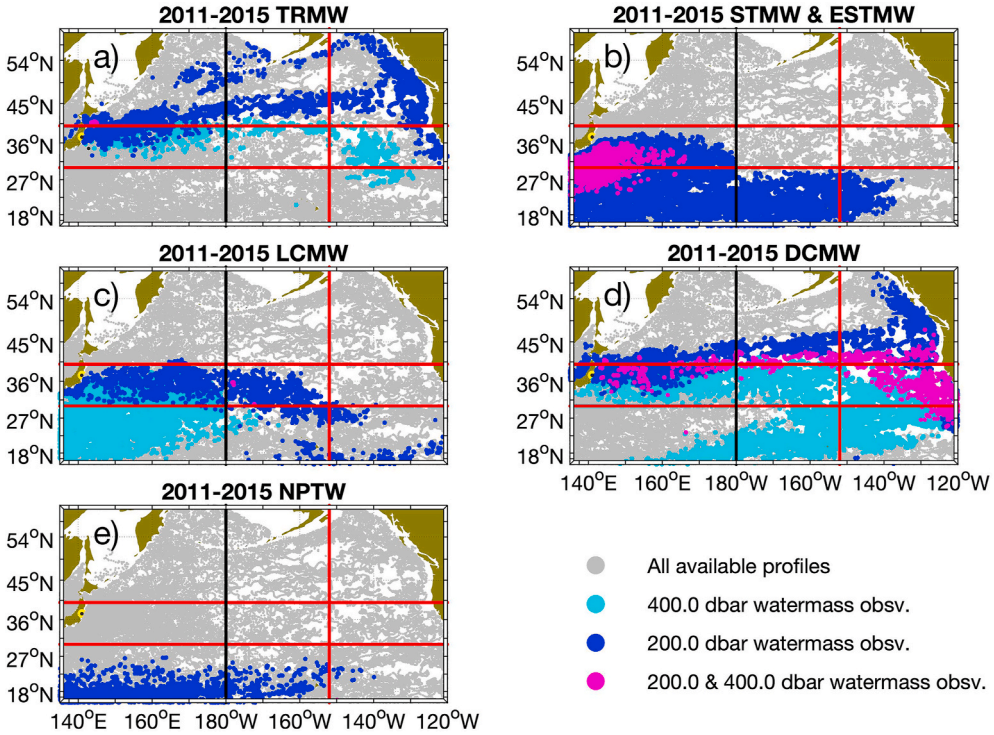

Fig. 8. Same as Fig. 8 except showing all available Argo profiles between March 2011 and June 2015 (gray dots) with the specified water mass characteristics at 200 dbar (dark blue dots), 400 dbar (light blue dots), and both 200 dbar and 400 dbar (pink dots). (For interpretation of the references to color in this figure legend, the reader is referred to the Web version of this article.)

is so much overlap in definitions that comparison among contributions is not possible. Neither of these results is surprising given the number of Cs observations that do not overlap with the water mass rectangles outlined in Fig. 6 and the extreme overlap in density definitions found in Table 1. Therefore, we use σ_0 along with the broad water mass latitudinal limits that were identified using the Argo profile data (Section 3.1), i.e. 30°N for subtropical and tropical waters and 32°N for L-CMW. With these criteria 74% of the 152°W water column is captured.

The ^{134}Cs inventory to the south of 30°N (Fig. 9b) is unreliable as there are few Cs samples and only one detected ^{134}Cs value. Further,

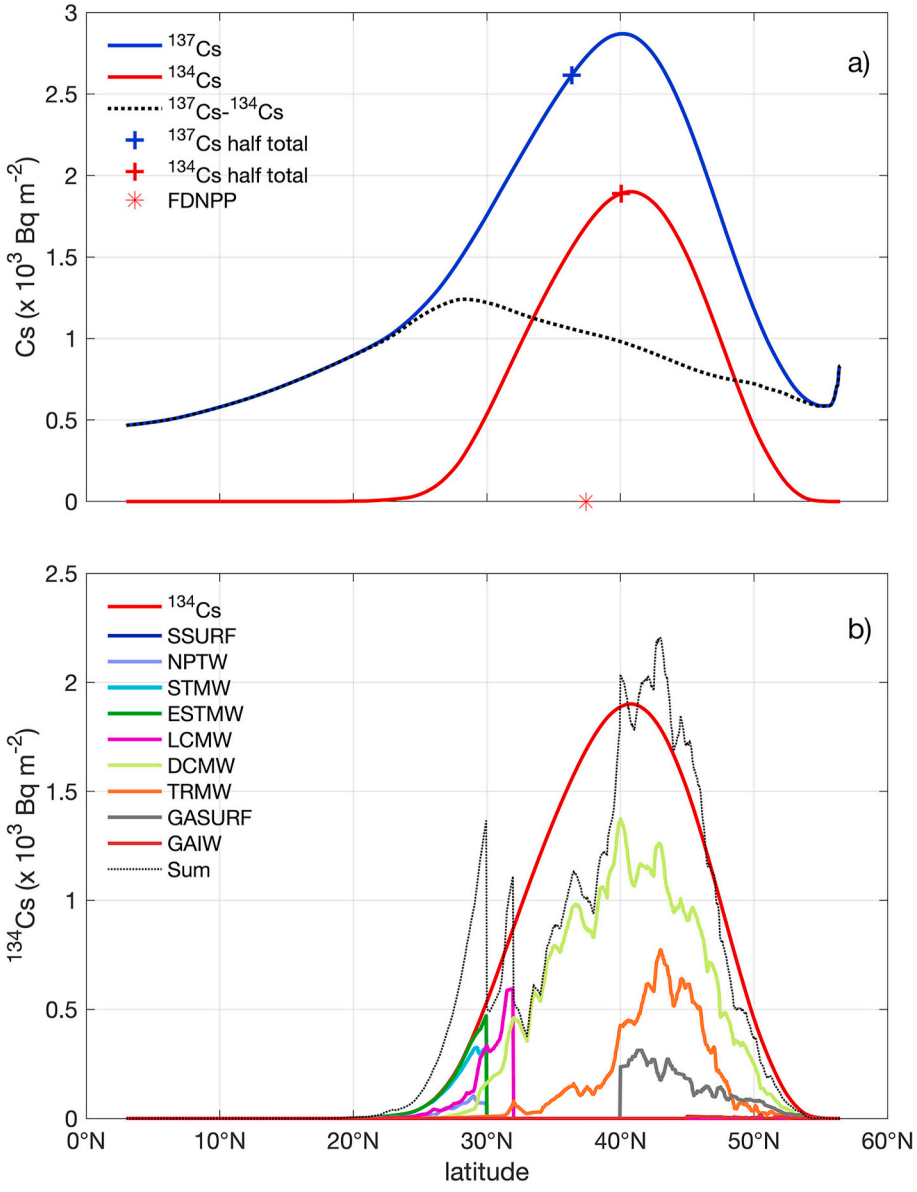

Fig. 9. a) Blue solid, red solid and black dotted curves indicate the water column inventory of ^{137}Cs, ^{134}Cs, ^{137}Cs-^{134}Cs in each square meter along the meridional 152°W line. Crosses indicate location where half the total inventory has been accumulated integrating from south to north. For ^{134}Cs this halfway point (40.05°N) almost coincides with maximum inventory (40.75°N). For ^{137}Cs the halfway point (36.35°N) is offset from the maximum (40.15°N). Red asterisk indicates FDNPP latitude; b) ^{134}Cs - red curve is the same as in (a), other colored curves represent the water column inventory component for each of the water masses discussed in the text. The dotted blue curve represents the sum of all water mass components. Note, due to overlap in water mass definitions the sum can be greater than the total. Likewise, because not all water is represented by these water masses the sum can be less than the total. All values are decay corrected to April 6, 2011. (For interpretation of the references to color in this figure legend, the reader is referred to the Web version of this article.)

while θ/S are available south of 30°N, the overlap in density limits means there is little one can say about which water mass is responsible for bringing the one small Cs signal to the line other than the general conclusion that ^{134}Cs is present in lighter subtropical waters. Between 30°N and 32°N, the effect of both CMWs becomes evident as L-CMW and D-CMW together account for all the Cs_F present. The prescribed 32°N cutoff in L-CMW (Fig. 9b pink curve) is clearly non-physical, and between 32°N and 40°N we are missing a significant portion of the water column with the latitude-σ_0 criteria (difference between the solid red and black dotted curves) as not all water masses present are accounted for in the definitions used.

If the formation region θ, S, and σ_0 are used to identify the L-CMW contribution, the cutoff is still at 32°N, but using σ_0 alone, the sum of the D- and L-CMW contributions is one and a half times the total. Therefore, for the purpose of this inventory calculation we define the missing portion as modified CMW, which is either spicier (i.e. warmer and saltier) than newly formed D-CMW (expanding the purple Fig. 6 rectangle up and to the right) and/or less spicy (i.e. cooler and fresher) than newly formed L-CMW (expanding the orange Fig. 6 rectangle down and to the left). With this modified CMW definition, of the ^{134}Cs signal at 152°W: 55% is associated with D-CMW, 5% is L-CMW defined to exist south of 32°N, 18% is modified CMW found between 32° and 40°N and another 18% is TRMW most of which is carried by waters to the north of 40°N. STMW and GASURF contribute 3% and 7%, respectively and as of 2015 at 152°W less 1% of the ^{134}Cs had made it into NPTW, SSURF and GAIW.

To compare to previous estimates, one needs an estimate of the total North Pacific inventory. We used the spring 2015 longitude limit of the Cs_F signal suggested by the Rossi et al. (2013) ensemble of simulations (see Section 3.5) to obtain a maximum western extent of 180°. To the east, we used the pattern of surface ^{137}Cs produced by Smith et al. (2017, their figure 4, June–August panel) based P16N data combined with observations from the summer 2015 Line-P and CCGS S. W. Laurier cruises. Along with a vertical distribution based on the 152°W observations and an assumed average Cs_{WT} of 1.5 Bq m^{-3} this produces a total North Pacific inventory (date corrected to April 6, 2011) of 13.3 PBq (7.1 PBq to the west of 152°W and 6.2 PBq to the east).

There are numerous uncertainties in this calculation. If the reach of the signal to the west were 10% more/less (to 176°E/176°W instead 180°) the total inventory estimate would increase/decrease by ~1 PBq. If the magnitude of the signal to the west were 10% more/less, the western component would be ~0.7 PBq larger/smaller. Distance matters

in the broad Pacific. If the signal core to the west lies closer to 40°N than 45°N, as does the core of the eastward flow, the inventory estimate could be ~0.6 PBq larger. A 10% larger core in the unobserved region to the southeast of 47°N, 152°W, could further increase the estimate by ~0.5 PBq. Therefore, a conservative range for the total ^{134}Cs inventory would be 11–16 PBq. This range is consistent with the previous estimates discussed, e.g. the DOD + AD estimates of 15–16 PBq (Inomata et al., 2016; Tsubono et al., 2016). How much AD and DOD individually contribute to this estimate depends on how much of each signal reached the 152°W line as sampled here.

In conclusion, based on the 152°W observations, the North Pacific Cs_F inventory is dominated by D-CMW and TRMW which together account for ~70% of the total. To rigorously combine the 2015 meridional dataset with observations taken at different times, geographic locations and depths to compute a total inventory is nontrivial. The physical processes involved (3-dimensional transport and dispersion) are associated with strong variability at monthly, seasonal and annual timescales making disentangling and/or correcting multiple datasets to

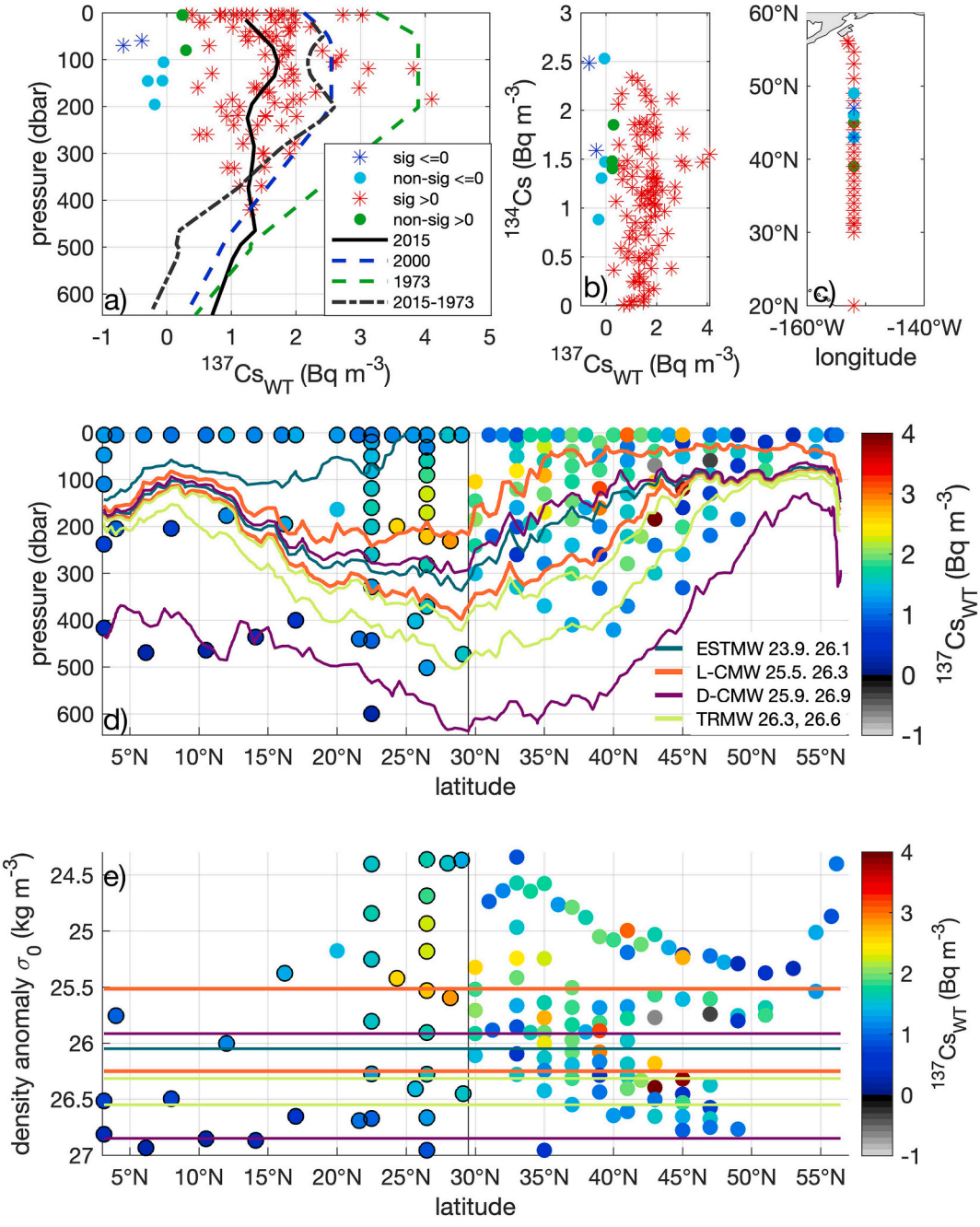

Fig. 10. Estimates of 152°W ^{137}Cs background calculated as $^{137}Cs_{WT}$ = observed ^{137}Cs minus predicted ^{137}Cs (calculated from ^{134}Cs observations and a decay corrected ^{137}Cs/^{134}Cs ratio). a) Asterisks (circles) are values that are (not) significantly different from zero, where significant implies a 95% confidence level. Red/green (blue/cyan) symbols are greater (less) than 0. Black solid line is the weighted mean of the red asterisks. Historical estimates shown as green and blue dashed curves are explained in the text. Gray dot-dash curve is the green minus the black curves; b) Comparison of ^{134}Cs to $^{137}Cs_{WT}$ magnitude, same symbols as in (a); c) geographical location of the symbols in (a); d) latitude-pressure section of significant $^{137}Cs_{WT}$ (i.e. red asterisks in (a)) plus to the south 30°N (see separating black line), observed ^{137}Cs (circled in black) at locations where no ^{134}Cs was detected^{137}Cs. Color contours represent water mass boundaries as in Fig. 3; e) Same as (d) in potential density anomaly-latitude space. (Units: Bq m^{-3}). (For interpretation of the references to color in this figure legend, the reader is referred to the Web version of this article.)

construct an "aggregated dataset" is a complex task. That said, a related project is presently underway to combine the many ocean Cs observations now available (MARIS, 2019) to investigate the inventory distribution throughout the full basin.

3.3. Background ^{137}Cs

By focusing on the ^{134}Cs results, we have thus far avoided making a distinction between the weapons testing ^{137}Cs ($^{137}Cs_{WT}$) background and the more recent FDNPP contamination. Here, we turn our attention to $^{137}Cs_{WT}$. Note that in the following discussion, if a specific reference year is not provided (e.g. "in year value was"), values are decay corrected to April 2011.

In 1980, Bowen et al. published estimates of $^{137}Cs_{WT}$ based on a zonal GEOSECS section and between 30°N and 35°N from 140°E to 120°E (i.e. crossing 152°W and henceforth referred to as GZ for GEOSECS Zonal) and a meridional section between 120°W and 128°W from 15°S to 35°N (henceforth GM), east of our section but covering some of the same latitudes (Fig. S7). On GZ at 152°W, ^{137}Cs observations suggested near surface values in 1973 of ~8.5 Bq m^{-3}, and a subsurface maximum at 50–150 m of ~10 Bq m^{-3} that decreased to 5 Bq m^{-3} by 500 m and to less than 0.3 Bq m^{-3} by ~600 m. On GM there was a fairly linear decrease with latitude at the surface from the 8.5 Bq m^{-3} at 30–35°N to somewhere in the range of 1.7–3.4 Bq m^{-3} at the equator. The vertical gradient was steeper further south (~5 Bq m^{-3} at 200 m and less than 0.3 Bq m^{-3} at 300–400 m between 0° and 15°N).

Ignoring mixing and advection for now, by 2011 the surface values on GZ at 152°W would have decayed to 3.5 Bq m^{-3} and the subsurface maximum to 4.3 Bq m^{-3} (Fig. 10a, green dashed curve). Consistent with the P16N observations (Fig. 3b), the decay corrected Bowen et al. (1980) vertical gradient implies 2011 values of less than 0.1 Bq m^{-3} at ~600 m. Livingston and Povinec (2000) reported a northeast Pacific surface ^{137}Cs value of 3 Bq m^{-3} in 2000, which decay corrected would be 2.3 Bq m^{-3} in 2011, or about a two-thirds of the decay corrected Bowen et al. (1980) value. Subtracting this fractional difference between the two surface estimates from the Bowen curve (Fig. 10a, green dashed curve) as a multiplicative offset, gives a profile estimate for 2000 (Fig. 10a, blue dashed curve) that assumes the shape of the profile did not change over time.

Here we have the opportunity to estimate the shape of the background field from the 2015 observations. By decay correcting 2011 FDNPP $^{134}Cs/^{137}Cs$ ratio (1.0, Buesseler et al., 2011) to spring 2015 and applying it to our ^{134}Cs observations a predicted FDNPP-only ^{137}Cs estimate can be obtained. The background $^{137}Cs_{WT}$ estimate is the difference between the observed and predicted ^{137}Cs (Fig. 10a, colored symbols and black solid curve). We estimate the mean (cross-section area-averaged) 2011 northeast Pacific $^{137}Cs_{WT}$ to be 1.2 ± 0.1 Bq m^{-3} (1.3 ± 0.1 Bq m^{-3} along 152°W, 1.1 ± 0.1 Bq m^{-3} across the gyre, and 0.34 ± 0.1 Bq m^{-3} in the surface waters along the short underway section off the coast of Seattle).

Comparing the patterns $^{137}Cs_{WT}$ (Fig. 10) suggest first that: a) the subsurface maximum vertical gradient reported by Bowen et al. (1980) still exists and in 2015 was on average 2 Bq m^{-3} at ~100 m; b) the surface latitudinal gradient they suggested may also still exist beginning at ~45°N; c) while south of 35°N the surface values are generally less than 2 Bq m^{-3}, the decay corrected Livingston and Povinec (2000) value and maximum surface values are slightly higher than this estimate; and d) while the magnitude of $^{137}Cs_{WT}$ is not dependent on the magnitude of the measured ^{134}Cs signal (Fig. 10b), the spread in $^{137}Cs_{WT}$ decreases with decreasing ^{134}Cs,.i.e. increasing depth. This last, speaks both to the latitudinal limits on the ^{134}Cs signal at depth and to the relationship between the 4- and 40-year mixing timescales.

The difference between the mean profiles suggested by data from the 1970's, the 1990's and 2015 is a result not only of the uncertainties in the estimates themselves but also mixing and stirring over time. Over the last 43 years the rate of non-decay related change in $^{137}Cs_{WT}$ (Fig. 10a, gray dot-dash curve = green curve minus black curve, henceforth $\Delta^{137}Cs_{WT}$) has developed a shape, which like the pattern of Cs_F, is at least partially related to the mixing and advection of western basin waters. While above ~50 m, lighter waters such as ESTMW dominate (Fig. 10d, above upper orange contour) and from 50 to 200 m, L-CMW contributes (below upper orange contour), the difference (the bulge in the gray dot-dash curve centered at about 100 m) is not significant. If one assumes that south of 30°N (black line Fig. 10d and e) where ^{134}Cs is not detectable, the distribution of ^{137}Cs (values circled in black Fig. 10d and e) represents $^{137}Cs_{WT}$, the same conclusion holds –waters just at and above L-CMW dominate even as the isopycnals descend southward.

Between 1973 and 2015 the mean $\Delta^{137}Cs_{WT}$ above 200 m has been 0.55 ± 0.02 Bq m^{-3} decade^{-1}. From 200 to 450 m (the deepest at which multiple ^{134}Cs observations are available) the mean $\Delta^{137}Cs_{WT}$ is 0.35 ± 0.15 Bq m^{-3} decade^{-1} and is associated with a steady decrease between the two depths of 14 ± 7 Bq m^{-3} decade^{-1} km^{-1}. As this slope is solely dependent on the Bowen et al. (1980) 1973 values (the 2015 observations suggest the 200–500 m $^{137}Cs_{WT}$ is well-mixed), it suggests that western basin mixing in the transition region into which Cs_F was discharged has been deeper/denser than that seen on average over the last 40 years. The lack of significant gradient with depth in $\Delta^{137}Cs_{WT}$ above 200 m (mid-range of western basin transition region winter MLD, Fig. S7), suggests that in the mean for these waters mixing on the 40-year and 4-year time scales are more similar. This result is consistent with Aoyama et al. (2008) who found subsurface maxima in $^{137}Cs_{WT}$ at 165°N in STMW and L-CMW.

3.4. What ^{90}Sr can and cannot tell us

Strontium-90 (28.79-year half-life) was also measured at some of the same locations as Cs on the 152°W line (Fig. 11, S8a-e). Like ^{137}Cs, there are two sources of ^{90}Sr, namely FDNPP ($^{90}Sr_F$) and weapons testing fallout ($^{90}Sr_{WT}$). The latter has a $^{137}Cs/^{90}Sr$ ratio of 1.46 ± 0.16 (Bowen et al., 1980) and an average surface ocean ^{90}Sr activity of ~1 Bq m^{-3} (Povinec et al., 2012). The 2011 $(^{137}Cs/^{90}Sr)_F$ ratio was much higher (~1000, Castrillejo et al., 2015) for AD due to the low volatility of Sr relative to Cs and 39 ± 1 ratio for DOD (Casacuberta et al., 2013; Buesseler et al., 2017). Although the AD and DOD ratios are different, observed levels of ^{137}Cs were not large enough to distinguish AD and DOD fractions (Figs. S8f–g).

The highest 2015 152°W ^{137}Cs activities are order 10 Bq m^{-3}. Assuming this 10 Bq m^{-3} of $^{137}Cs_F$ has been added to the existing system, then it follows that with $(^{137}Cs/^{90}Sr)_F$ ratios of 1000 and 40, an additional 0.01 and 0.25 Bq m^{-3} of ^{90}Sr from AD and DOD would be observed, respectively. Given the ^{137}Cs and ^{90}Sr detection limits (see Section 2.2, and note no Cs samples sent to HADES Lab Cs measured ^{90}Sr) and the 152°W surface background levels of 1–2 Bq m^{-3} for ^{137}Cs and ~1.3 Bq m^{-3} for ^{90}Sr, we can conclude that additional $^{90}Sr_F$ would not be seen in the measured $^{137}Cs/^{90}Sr$ ratio. Consistent with this conclusion, only one sample had ^{90}Sr elevated over background by more than the associated measurement error (Fig. S8f). If instead we assume that all measured ^{90}Sr came from weapons testing, we can take advantage of the constant $^{137}Cs/^{90}Sr$ ratio (Fig. S8g) in that source to calculate the $^{137}Cs_{WT}$ and derive the $^{137}Cs_F$ component by differencing the observed ^{137}Cs and estimated $^{137}Cs_{WT}$. This technique is similar to that used in Section 3.3. In fact, the ^{90}Sr method has a smaller associated error and can therefore be more useful than the $^{137}Cs/^{134}Cs$ method deeper in the water column where radionuclide activities are low (Fig. 11a). The ^{90}Sr technique suggests similar latitudinal and density gradients in $^{137}Cs_{WT}$ (Fig. 11b). In the near future, when ^{134}Cs has decayed beyond measuring capabilities, ^{90}Sr may be the only way to satisfactorily separate $^{137}Cs_{WT}$ from $^{137}Cs_F$.

3.5. Comparison to model predictions

Based on observed density surfaces and the modeling work of

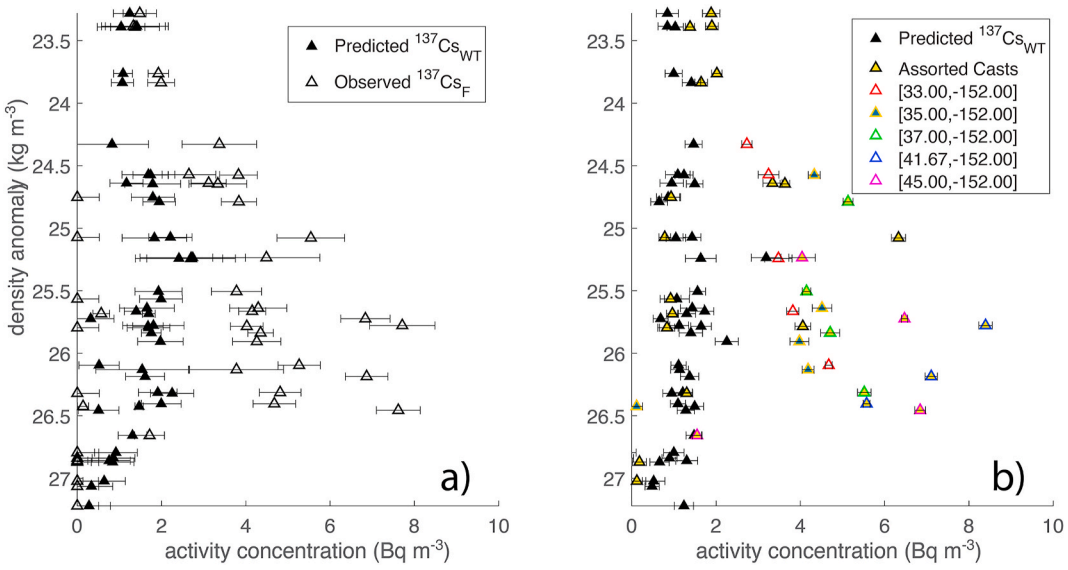

Fig. 11. ^{137}Cs predicted from: a) observed ^{134}Cs (method explained in Section 3.3) and b) ^{90}Sr (method explained in Section 3.4). Solid triangles indicate predicted $^{137}Cs_{WT}$ estimates and open triangles indicate observed $^{137}Cs_F$. Colors in (b) represent predicted values at different latitudes along the 152°W line. Note, here values are decay corrected to the day of collection. These profiles are shown individually in Fig. S8. (For interpretation of the references to color in this figure legend, the reader is referred to the Web version of this article.)

Behrens et al. (2012), it was hypothesized that deep winter mixing in the western basin and subsequent eastward advection along isopycnal surfaces within the ocean interior would produce subsurface Cs_F maxima in our eastern basin observations. The depth of these maxima would depend on the ventilation intensity, i.e. the depths of winter mixed layers that occurred following the discharge. A more complete scenario would be that the predominant surface advection associated with intense mixing through a rich eddy field would be the main dynamics responsible for the first (2012–2016) invasion of surface intensified Cs_F maxima in the eastern basin. Later (2014–2021), Cs-enriched MWs formed in the western basin during the previous winters would reach the subsurface Northeast Pacific through complex 3-dimensional pathways (Rossi et al., 2013, 2014; henceforth RET1314). The RET1314 simulations suggested that tracer concentrations would be primarily determined by the mixed layer concentrations at the time and location of MW formation, while the presence or absence of observed tracer along the sampled section would be mainly determined by the small-scale variability of interior pathways. In the Northeast Pacific, the model predicted surface $^{137}Cs_F$ maxima of the order of 10 Bq m^{-3} to the north of 40°N throughout 2012–2016 period, while subsurface maxima of order of 1 Bq m^{-3} were suggested south of 40°N over 2014–2021 period (RET1314).

The RET1314 particle trajectory simulations based on the Ocean model For the Earth Simulator (OFES) eddy-resolving velocity fields, the most realistic in the region, provides an excellent qualitative of comparison between the 152°W observations and a model prediction (Fig. 12). Note, although we compare to model results extending to 2015, the model was not rerun for our comparison. The RET1314 model tracer is FDNPP DOD $^{137}Cs_F$. The simulations used a 22 PBq point source (larger than our DOD + AD inventory estimate, Section 3.2) within 30 km of the FDNPP, assumed no background Cs_{WT} and neglected AD. Despite these acknowledged limitations, there are many qualitative similarities between the observed and simulated 152°W Cs_F signals: the latitudinal distributions as of May 2015 (Fig. 12a) are centered in generally similar location (~25–50°N, Fig. 12b and c); they extend to a similar depth (~600 m, Fig. 12b and c); the maximum activity is the same order of magnitude (~10 Bq m^{-3} compared to observed $^{137}Cs_F$+$^{137}Cs_{WT}$ of ~12 Bq m^{-3}); and maximum signal lies subsurface in the upper water column but includes a surface signature. That said, on closer inspection a number of both qualitative and quantitative differences become apparent.

While the maxima are similar, the source estimates for the model (22 PBq) and observations (11–16 PBq) are different. Scaling the model maximum by the ratio of the estimated source sizes results in a model prediction (~5–7 Bq m^{-3}) that is half what is observed. Also, the 152°W distribution details are different. While the model distribution of $^{137}Cs_F$ contains pockets of higher subsurface values at about 37°N, 41°N, and possibly, 47°N at 50–125 m (Fig. 12a, northern circles), the major core lies to the south at 30–35°N, 0–100 m (Fig. 12a rectangle) and the maximum lies very close to the surface (upper right corner of rectangle and southernmost circle). The observed maximum core lies at 41–44°N 0–200 m with a maximum at 100 m (Figs. 3b and 12b). Note, however, that due to the differences in magnitude there are few locations where simulated values are greater than observed values (Fig. 12c).

The above $^{137}Cs_F$ comparison provides insights into the "bigger picture" and continuity with the earlier literature – RET1314 and others who discuss these works, but comparing observed and modeled $^{134}Cs_F$ is more rigorous because there is no measurable $^{134}Cs_{WT}$. Applying the same $^{134}Cs/^{137}Cs$ ratio used in Section 3.3 to the RET1314 estimates highlights the differences between the modeled particle trajectory results and the observations (Fig. 12b). The observed $^{134}Cs_F$ (maximum of ~10 Bq m^{-3}) is significantly greater than that modeled (~3.5 Bq m^{-3}, or 1.8 -to 2.5 Bq m^{-3} scaling by estimated source size ratio) resulting in observed minus modeled differences that are positive everywhere in the region of the cores (Fig. 12c).

The differences in the center of the stronger southern modeled core (30°-35°N) are actually somewhat less than those found to the north because the mid-range observed signal has about the same magnitude as the most intense modeled values. There is not only a north/south offset in the location of the core (see the offset of the inner black contour from the darkest shaded circles in Fig. 12c), but the modeled signal is also more diffuse than the observed, particularly to the south where there is no indication of the observed ^{134}Cs 30°N cutoff (see southward extension of the outer black contour (Fig. 12c). To the north, we note that the Alaska Current signal is missing from the model (Fig. 12b, see shaded circles north of 50°N). The specific dynamics that would go into explaining the mismatches are not straightforward because as emphasized by Rossi et al. (2013), the processes that produce the distribution depend both on remote effects (e.g. three-dimensional MW pathways and tracer concentration, primarily acquired at the time and location of

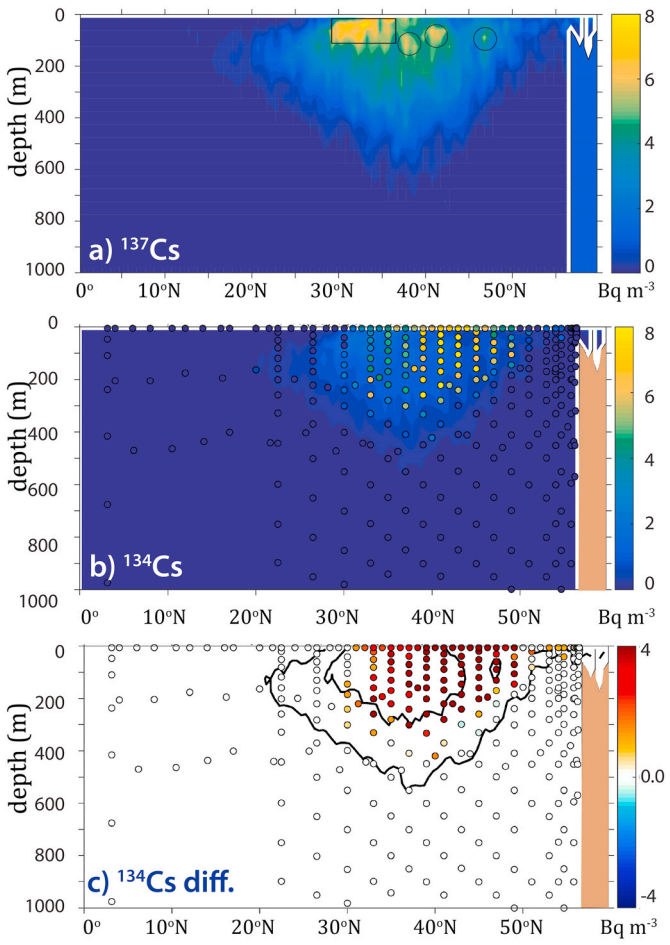

Fig. 12. a) Model simulation estimate of May 2015 distribution of ^{137}Cs along the meridional 152°W line, black rectangle and circles highlight higher activity cores mentioned in the text; b) the same as (a) but for ^{134}Cs calculated using ^{134}Cs/^{137}Cs ratio decay corrected to 2015, shaded black/empty white circles indicate observed values and non-detectable samples; c) shaded black circles indicate the observed minus model ^{134}Cs differences, empty green circles indicate non-detectable samples, black contours are isolines of ^{134}Cs, where the outer line (0.25 Bq m^3) broadly represents the edge of model simulated plume and the inner line (1.0 Bq m^3) highlights the core of the simulated plume. Note, -8 to 8 Bq m^3 color axis highlights the positive nature of these differences. (For interpretation of the references to color in this figure legend, the reader is referred to the Web version of this article.)

MW formation) and on local effects (e.g. upwelling strength, mean depth of upwelling sources, local lateral advection and mixing (see also Smith et al. (2017)).

Modeled vs. actual velocity fields: The latitudinal locations of the Kuroshio, the KE and KBF and the diffusive nature of the model are all likely reasons for the differences between the observed and modeled distributions. The modeled results indeed consist of an ensemble of simulations (averaging out the pathways of multiple years of currents (1980–2008), i.e. multiple latitudinal locations of the core axes) and multiple years of western basin water mass formation that do not include those from the actual 2011–2015 period. It is the "ensemble approach" that produces an overall more diffuse pattern and contributes to the pronounced southward extension of the modeled cores along 152°W as it "aggregates" different cores together, allowing for more opportunities for crossing the subtropical and subpolar gyre boundaries before arrival in the eastern basin.

Modeled vs. actual water mass formation: A possible contributor to the more southerly model Cs_F core is that between 1980 and 2008 more modeled L-CMW formed in the transition region (Fig. 1) than between 2011 and 2012 (Kumamoto et al., 2014; Kaeriyama et al., 2016; Cedarholm et al., 2019), which would result in a more southerly eastward flow of Cs_F (Oka and Qiu, 2012). This highlights the non-negligible role of the prominent inter-annual variability of MW formation and its effect on our understanding of the long-term fate of oceanic tracers and properties.

Modeled vs. actual tracer source: Another difference between modeled and observed Cs distributions is that the model did not include an AD source as it was poorly understood at the time the model runs were performed. The fact that the southern core in the model is overestimated suggests that modeled L-CMW has carried a substantial portion of the DOD signal across the basin. The region of maximum AD was to the northwest of the FDNPP (e.g. Stohl et al., 2012), that is, in the region of denser D-CMW/TRMW formation. Therefore, by neglecting such surface inputs, the model underestimates the northern core as compared to the strong D-CMW signal seen in the observations. Following this train of thought, it suggests that AD may be the dominant source of the 152°W signal.

RET1314 projected that the portion of $^{137}Cs_F$ that had been subducted into the interior ocean would return to the surface via coastal upwelling along the west coast of North America, some years after the initial surface report in 2012–2013 that was solely due to horizontal currents. They suggested that this process would take about 6–9 years after DOD, that is 2017–2021 (later than 2015). If, as discussed above, the bulk of modeled signature was advected in L-CMW on the inside edge of the subtropical gyre, rather than D-CMW/TRMW on the outside edge, its arrival in the north would have be slowed. It is also interesting to consider the lone ^{134}Cs observation obtained at 20°N. The model, like the observations, finds the tracer signal to be subsurface at this latitude, and as the model does not include AD, its signal cannot be AD mixed down into ESTMW in 2011, but must instead have been DOD advected in lighter waters.

It is worth noting that other factors contributing to the differences are the patchiness of tracer distributions in the real ocean associated with the discrete and non-synoptic sampling that could bias the "observational" perspective. Indeed, if a southern core exists, it is possible that the sampling missed it due to submesoscale variability in the real ocean. From this perspective, our model-data comparison highlights how the model prediction and observations complement each other to reconstruct the "true" tracer fate.

4. Summary and conclusions

In 2015, nearly 400 individual samples for measurement of radionuclides (^{134}Cs, ^{137}Cs, ^{90}Sr) were collected along 152°W, across the Alaska Gyre and on a 200 nautical mile transect in the EEZ off Seattle. The samples presented maximum magnitudes, decay corrected to April 2011, of order of 10 Bq m^{-3} (^{134}Cs), 12 Bq m^{-3} (^{137}Cs) and 2.5 Bq m^{-3} (^{90}Sr). These radionuclide tracers carry a signature of MW formed in the northwest 3–4 years earlier after they had traversed some 7500 km beneath the surface to arrive at 152°W. Here, these waters penetrate to about 300 m at 30°N, 400 m at 40°N, and shoal with the density surfaces that rise toward the North American coast. Covering the distance between the FDNPP and 35°N, 152°W (location of deepest ^{134}Cs) in 4 years suggests a cross-basin advection speed that averages about 4.8 cm s^{-1}. This is faster than the mean western basin 3 cm s^{-1} reported by Oka et al. (2011), but similar to the estimates reported by Kumamoto et al. (2019) for ^{137}Cs export from the western basin in 2011. Interestingly, it is also similar to the 4.6 cm s^{-1} reported by Taguchi and Schneider (2014) as the average 0–400 m eastward propagation speed of ocean heat content anomalies crossing the basin between 40°N and 48°N (see their figure 1). This comparison brings the discussion full circle – back to one motivation for this study mentioned in the introduction (Section 1.1): information about MW circulation gleaned from Cs_F could be useful to our understanding of MW impacts on other surface-related variables such as oxygen utilization, carbon uptake and storage rates, as well as

sea-surface temperature variability.

The observations suggest that more than half the Cs_F was brought to 152°W in D-CMW with significant, but smaller, contributions supplied by TRMW, L-CMW, and a modified version of either or both varieties of CMW. There was a clear cutoff in the Cs_F signature at 30°N, the estimated northern limit of subtropical and tropical waters, indicating that CMW's stayed within the North Pacific Current over this time frame and did not diffuse southward west of this longitude. This result is consistent with analysis of Argo float profiles, but inconsistent with the model-based particle trajectory experiments of Rossi et al. (2013, 2014). The core of the strongest Cs_F signal (39°-45°N) extended from just below the surface to ~260 m. Cs_F observations also indicated transport of a weak surface signal around the Alaska Gyre in the boundary current and an upwelling of Cs_F near the Seattle coast, which is consistent with Line-P findings (e.g. Smith et al., 2015, 2017). The 152°W observations suggest a basin-wide 2011 Cs inventory of 11–16 PBq.

The ^{137}Cs observations support the results found using FDNPP fingerprint of ^{134}Cs and also provide some information about the weapons testing background. Using all P16N ^{134}Cs measurements we find a mean 2011 Northeast Pacific $^{137}Cs_{WT}$ activity of 1.2 ± 0.1 Bq m^{-3} (at 152°W the mean $^{137}Cs_{WT}$ is 1.3 ± 0.1 Bq m^{-3}). Over the last half century, this weapons signal has penetrated down to 900–1000 m in the Alaska Gyre (the deepest detection between 37°N and 50°N) and to ~400 m throughout the subtropical gyre and into the tropics. Earlier studies reported a latitudinal dependence for $^{137}Cs_{WT}$ in the Northeast Pacific and the 2015 Cs and Sr both suggest that this dependence, although weaker than a few decades ago, appears to have been retained.

The analysis of 152°W 2015 Cs suggests that it was the denser variety of mode waters (D-CMW/TRMW) that brought most of the signal eastward. Analyses of ARGO floats show that this is because there was formation of denser than usual waters in the transition region in the 2011–2012 timeframe. As observed by others (e.g. Inomata et al., 2018; Aoyama et al., 2016a), these waters were advected into the North Pacific Current. The comparison to the DOD based simulations of RET1314 suggests that this D-CMW/TRMW signal may also be attributable to western basin AD, rather than DOD. Although some evidence of L-CMW (commonly formed in the transition region) is seen at 152°W, with the clear cutoff in the Cs_F at 30°N (the boundary with both E-STMW and subtropical gyre waters) it is likely that the bulk of Cs_F in L-CMW was subducted and advected eastward on southern side of the KE, and drawn into the western basin recirculation. Unlike Cs_F (4-year timescale), weapons testing background (50-year timescale) does appear to be associated with L-CMW. This result is consistent with analysis of observations at 165°E (Aoyama et al., 2008).

The release of Cs_F has afforded the opportunity to employ a powerful, soluble, readily detectable tracer discharged into the ocean at a known time and location to better understand North Pacific dynamics. Moving beyond the question of the extent and speed with which FDNPP radioactivity has spread, we have begun to examine what this unique tracer can tell us about the underlying physical processes and evolution of the 2011 vintage of MWs. Future efforts will look to combine these 2015 observations with other data collected across the basin as well as model output and non-radionuclide water property observations. Together, these data will allow investigation into the role of North Pacific MW in transporting, mixing and storing the characteristics they gain from the atmosphere at the time of formation and will improve our understanding of the MW role in the cycles associated with ocean heat content, biological production, nutrient cycling as well as CO_2 uptake and ocean acidification.

Declaration of competing interest

The authors declare that they have no known competing financial interests or personal relationships that could have appeared to influence the work reported in this paper.

Acknowledgements

We thank the science parties and crew of the National Oceanic and Atmospheric Administration (NOAA) ship Ronald Brown, which occupied the 2015 repeat of the P16N line, for their assistance in obtaining water samples for radiocesium measurement. In particular, we thank Samantha Siedlecki, leg 1 co-chief scientist, for her assistance in obtaining the 27 samples to the south of Hawaii, Jessica Cross, leg 1 chief scientist, for her diplomatic assistance with logistics in Tahiti, and Brendan Carter for discussion on inventories. All WHOI-based co-authors acknowledge salary and project support from the National Science Foundation (NSF) grant OCE#-1356630 and OCE#-1923387. Pike's participation in the 2015 P16N cruise was supported through this same grant and Macdonald's participation was supported by NSF grant OCE#-1437015. We acknowledge additional salary support for Buesseler from the Deerbrook Charitable Trust (grant# DCT 17-30) and Kenyon from an NSF Graduate Research Fellowship under grant #1122374. Rossi acknowledges Australia's University of New South Wales (UNSW) as some modeling aspects of this research were generated using the Linux computational cluster Katana supported by the Faculty of Science at UNSW. We thank the personnel at the HADES Underground Laboratory (HADES, 2020) for their efforts in providing us with low-level isotope measurements. The HADES work was supported by the European Commission Joint Research Center within HORIZON2020 via the European Atomic Energy Community (EURATOM) open access scheme EUFRAT for transnational access (project number 8-15). We wish to acknowledge the more than 350 individuals and groups who contributed to the Our Radioactive Ocean crowd funding campaign (ORO, 2013) and the collaborative efforts of personnel from both NOAA and NSF for making it possible for us to obtain the two extra days of ship time needed to perform the Cs-only casts on P16N. No analysis of these data was performed while onboard the NOAA vessel. Last, but no means least, we extend our sincere thanks to our reviewers and the journal's editor-in-chief, all of whom gave us the gift of careful reading, thoughtful critique and astute insights.

Appendix A. Supplementary data

Supplementary data to this article can be found online at https://doi.org/10.1016/j.dsr.2020.103379.

Data sources and availability

The P16N dataset, including the Cs measurements, was collected through the U.S. GO-SHIP program (https://usgoship.ucsd.edu/) and made freely available through CCHDO (2019). The Cs measurements have also been contributed to MARIS (2019) through which they are also freely available. The Argo float profiles were collected and are made freely available by the International Argo Program and the national programs that contribute to it. (http://www.argo.ucsd.edu, http://argo.jcommops.org). The Argo Program is part of the Global Ocean Observing System.

Contributions

A. Macdonald organized the collection of the P16N Cs data set, performed the physical analysis of the Cs data, wrote the manuscript and created all figures except those mentioned below. S. Yoshida, I. Rypina contributed in the physical analysis of the Cs observations. S. Pike collected and shipped the P16N samples, measured many of the samples, produced the original Cs data set and wrote the section on the chemical analysis. J. Drysdale also measured samples, organized shipping of samples to HADES and calculated radiocesium estimates and uncertainties based on the HADES results. K. Buesseler led the chemical analysis and contributed to the chemistry described herein. S. Jayne contributed expertise on the mode water formation region and

Northwest Pacific circulation. V. Rossi provided the model-based particle tracking results and figures, and contributed to the text on the same. J. Kenyon provided the figures and contributed the text pertaining to ^{90}Sr. All co-authors contributed through comments, suggestions and the editing of the full manuscript.

References

Aarkrog, A., 2003. Input of anthropogenic radionuclides into the World Ocean. Deep-Sea Res. II 50, 2597–2606.

Aoyama, M., Hirose, D., 2008. Radiometric determination of anthropogenic radionuclides in seawater. In: Povinec, P.P. (Ed.), Analysis of Environmental Radionuclides, vol. 11, pp. 137–162.

Aoyama, M., Hirose, D., Nemoto, K., Takasuki, Y., Tsumune, D., 2008. Water masses labeled with global fallout 137Cs formed by subduction in the North Pacific. Geophys. Res. Lett. 35, L01604. https://doi.org/10.1029/2007GL031964.

Aoyama, M., Fukasawa, M., Hirose, K., Hamajima, Y., Kawano, T., Povinec, P.P., Sanchez-Cabeza, J.A., 2011. Cross equator transport of 137Cs from North Pacific ocean to South Pacific Ocean (BEAGLE2003 cruises). Prog. Oceanogr. 89, 7–16.

Aoyama, M., Tsumune, D., Hamajima, Y., 2012. Distribution of 137Cs and 134Cs in the North Pacific Ocean: impacts of the TEPCO Fukushima-Daiichi NPP accident. J. Radioanal. Nucl. Chem. https://doi.org/10.1007/s10967-012-2033-2.

Aoyama, M., Uematsu, M., Tsumune, D., Hamajima, Y., 2013. Surface pathway of radioactive plume of TEPCO Fukushima NPP1 released ^{134}Cs and ^{137}Cs. Biogeosciences 10. https://doi.org/10.5194/bg-10-3067-2013.

Aoyama, M., Hamajima, Y., Hult, M., Uematsu, M., Oka, E., Tsumune, D., Kumamoto, Y., 2016a. ^{134}Cs and ^{137}Cs in the North Pacific Ocean derived from the March 2011 TEPCO Fukushima Dai-ichi nuclear power plant accident, Japan. Part one: surface pathway and vertical distributions. J. Oceanogr. 72, 53–65. https://doi.org/10.1007/s10872-015-0335-z.

Aoyama, M., Kajino, M., Tanaka, T.Y., Sekiyama, T.T., Tsumune, D., Tsubono, T., Hamajima, Y., Inomata, Y., Gamo, T., 2016b. ^{134}Cs and ^{137}Cs in the North Pacific Ocean derived from the TEPCO Fukushima Dai-ichi nuclear power plant accident, Japan in March 2011: part two – estimation of ^{134}Cs and ^{137}Cs inventories in the North Pacific Ocean. J. Oceanogr. 72, 67–76. https://doi.org/10.1007/s10872-015-0332-2.

Aoyama, M., Inomata, Y., Tsumune, D., Tateda, Y., 2019. Fukushima radionuclides in the marine environment from coastal region of Japan to the Pacific Ocean through the end of 2016. Prog. in Nuclear Science and Technology 6, 1–7. https://doi.org/10.15669/pnst.6.1.

Argo, 2019. Argo information centre. http://www.argo.net/.

Behrens, E., Schwarzkopf, F.U., Lübbecke, J.F., Böning, C.W., 2012. Model simulations on the long-term dispersal of ^{137}Cs released into the Pacific Ocean off Fukushima. Environ. Res. Lett. 7 https://doi.org/10.1088/1748-9326/7/3/034004.

Bingham, F.M., Suga, T., 2006. Distributions of mixed layer properties in North Pacific water mass formation areas: comparison of Argo floats and World Ocean Atlas 2001. Ocean Sci. 2, 61–70.

Bowen, V.T., Noshkin, V.E., Livingston, H.D., Volchok, H.L., 1980. Fallout radionuclides in the Pacific Ocean: vertical and horizontal distributions, largely from GEOSECS stations. Earth Planet Sci. Lett. 49, 411–434.

Breier, C.F., Pike, S.M., Sebesta, F., Tradd, K., Breier, J.A., Buesseler, K.O., 2016. New applications of KNiFC-PAN resin for broad scale monitoring of radiocesium following the Fukushima Dai-ichi nuclear disaster. J. Radioanal. Nucl. Chem. 307, 2193–2200.

Buesseler, K.O., Aoyama, M., Fukasawa, M., 2011. Impacts of the Fukushima nuclear power plants on marine radioactivity. Environ. Sci. Technol. 45, 9931–9935.

Buesseler, K.O., Jayne, S.R., Fisher, N.S., Rypina, I.I., Baumann, H., Baumann, Z., Breier, C.F., Douglass, E.M., George, J., Macdonald, A.M., Miyamoto, H., Nishikawa, J., Pike, S.M., Yoshida, S., 2012. Fukushima-derived radionuclides in the ocean and biota off Japan. Proc. Natl. Acad. Sci. Unit. States Am. 109, 5984–5988. https://doi.org/10.1073/pnas.1120794109.

Buesseler, K.O., Dai, M., Aoyama, M., Benitez-Nelson, C., Charmasson, S., Higley, K., Maderich, V., Masqué, P., Morris, P.J., Oughton, D., Smith, J.N., 2017. Fukushima-derived radionuclides in the ocean: transport, fate, impacts. Annu. Rev. Mar. Sci. 2017 9, 173–203. https://doi.org/10.1146/annurev-marine-010816-060733.

Butler, D., 2011. Radioactivity spreads in Japan. Nature 471, 555–556. https://doi.org/10.1038/471555a.

Casacuberta, N., Masqué, P., Garcia-Orellana, J., Garcia-Tenorio, R., Buesseler, K.O., 2013. ^{90}Sr and ^{89}Sr in seawater off Japan as a consequence of the Fukushima Dai-ichi nuclear accident. Biogeosciences 10, 3649–3659. https://doi.org/10.5194/bg-10-3649-201.

Castrillejo, M., Casacuberta, N., Breier, C.F., Pike, S.M., Masqué, P., Buesseler, K.O., 2015. Reassessment of ^{90}Sr, ^{137}Cs, and ^{134}Cs in the coast off Japan derived from the Fukushima Dai-Ichi nuclear accident. Environ. Sci. Technol. 50, 173–180.

CCHDO, 2019. CLIVAR and carbon hydrographic data office. https://cchdo.ucsd.edu/.

Cedarholm, E.R., Rypina, I.I., Macdonald, A.M., Yoshida, S., 2019. Investigating subsurface pathways of Fukushima Cs in the Northwest Pacific. Geophys. Res. Lett. https://doi.org/10.1029/2019GL082500.

Chino, M., Nakayama, H., Nagai, H., Terada, H., Katata, G., Yamazawa, H., 2011. Preliminary estimation of release amounts of ^{131}I and ^{137}Cs accidently discharged from the Fukushima Daiichi Nuclear Power Plant into the atmosphere. J. Nucl. Sci. Technol. 48, 1129–1134.

Conkright, M.E., Locarnini, R.A., Garcia, H.E., O'Brien, T.D., Boyer, T.P., Stephens, C., Antonov, J.I., 2002. World Ocean Atlas 2001: Objective Analysis, Data Statistics and Figures CD-ROM Documentation. National Oceanographic Data Center, Silver Spring, MD, p. 17.

Dong, D., Brandt, P., Chang, P., Schütte, F., Yang, X., Yan, J., Zeng, J., 2017. Mesoscale eddies in the Northwestern Pacific Ocean: three-dimensional eddy structures and heat/salt transports. J. Geophys. Res. 122, 9795–9813. https://doi.org/10.1002/2017JC013303.

Garraffo, Z.D., Kim, H.-C., Mehra, A., Spindler, T., Rivin, I., Tolman, H.L., 2014. Modeling of ^{137}Cs as a Tracer in a Regional Model for the Western Pacific, after the Fukushima Daiichi Nuclear Power Plant Accident of March 2011. Weather Forecast. https://doi.org/10.1175/WAF-D-13-00101.1.

GODAS, 2015. National centers for envorimental prediction Global Ocean data Assimilation System (GODAS) monthly and annual mean products. https://www.cpc.ncep.noaa.gov/products/GODAS/monthly.shtml.

HADES, 2020. HADES underground laboratory. https://science.sckcen.be/en/Facilities/HADES.

Hautala, S.L., Roemmich, D.H., 1998. Subtropical mode water in the Northeast Pacific basin. J. Geophys. Res. 103, 13055–13066. https://doi.org/10.1029/98JC01015.

Holte, J., Talley, L., Gilson, J., Roemmich, D., 2017. An Argo mixed layer climatology and data base. Geophys. Res. Lett. https://doi.org/10.1002/2017GL073426.

Inomata, Y., Aoyama, M., Hirose, K., 2009. Analysis of 50-y record of surface ^{137}Cs concentrations in the global ocean using the HAM-global database. J. Environ. Monit. 11 (1), 116–125.

Inomata, Y., Aoyama, M., Tsubono, T., Tsumune, D., Hirose, K., 2016. Spatial and temporal distributions of ^{134}Cs and ^{137}Cs derived from the TEPCO Fukushima Daiichi nuclear power plant accident in the North Pacific Ocean by using optimal interpolation analysis. Environ. Sci. Process. Impacts 18, 126–136.

Inomata, I., Aoyama, M., Tsubono, T., Tsumune, D., Kumamoto, Y., Nagai, H., Yamagata, T., Kajino, M., Tanaka, Y.T., Sekiyama, T.T., Oka, E., Yamada, M., 2018. Estimate of Fukushima-derived radiocaesium in the North Pacific Ocean in summer 2012. J. Radioanal. Nucl. Chem. 318, 1587–1596. https://doi.org/10.1007/s10967-018-6249-7.

Kameník, J., Dulaiova, H., Buesseler, K.O., Pike, S.M., Šťastná, K., 2013. Cesium-134 and 137 activities in the central North Pacific Ocean after the Fukushima Dai-ichi nuclear power plant accident. Biogeosci. Discuss. 10, 5223–5244. https://doi.org/10.5194/bgd-10-5223-2013.

Kaeriyama, H., Shimizu, Y., Ambe, D., Masujima, M., Shigenobu, Y., Fujimoto, K., Ono, T., Nishiuchi, K., Taneda, T., Kurogi, H., Setou, T., Sugisaki, H., Ichikawa, T., Hidaka, K., Hiroe, Y., Kusada, A., Kodama, T., Kuriyama, M., Morita, H., Nakata, K., Morinaga, K., Morita, T., Watanabe, T., 2014. Southwest intrusion of ^{134}Cs and ^{137}Cs derived from the Fukushima Dai-ichi nuclear power plant accident in the western North Pacific. Environ. Sci. Technol. 48, 3120–3127.

Kaeriyama, H., Shimizu, Y., Setou1, T., Kumamoto, Y., Okazaki, M., Ambe, D., Ono, T., 2016. Intrusion of Fukushima-derived radiocaesium into subsurface water due to formation of mode waters in the North Pacific. Sci. Rep. 6 https://doi.org/10.1038/srep22010.

Katsura, S., Oka, E., Qui, B., Schneider, N., 2013. formation and subduction of North Pacific tropical water and their interannual variability. J. Phys. Oceanogr. 43, 2400–2415.

Katsura, S., 2018. Properties, formation, and dissipation of the North Pacific Eastern Subtropical mode water and its impact on interannual spiciness anomalies. Prog. Oceanogr. 162, 120–131. https://doi.org/10.1016/j.pocean.2018.02.023.

Kawakami, Y., Sugimoto, S., Suga, T., 2016. Inter-annual zonal shift of the formation region of the lighter variety of the North Pacific Central Mode Water. J. Oceanogr. 72, 225–234. https://doi.org/10.1007/s10872-015-0325-1.

Kouketsu, S., Kaneko, I., Kawano, T., Uchida, H., Doi, T., Fukasawa, M., 2007. Changes of North Pacific intermediate water properties in the subtropical gyre. Geophys. Res. Lett. 34 https://doi.org/10.1029/2006GL028499.

Kumamoto, Y., Aoyama, M., Hamajima, Y., Aono, Y., Kouketsu, S., Murata, A., Kawano, T., 2014. Southward spreading of the Fukushima-derived radiocesium across the Kuroshio extension in the North Pacific. Sci. Rep. https://doi.org/10.1038/srep04276.

Kumamoto, Y., Aoyama, M., Hamajima, Y., Nishino, S., Murata, A., Kikuchi, T., 2016. Meridional distribution of Fukushima-derived radiocesium in surface seawater along a trans-Pacific line from the Arctic to Antarctic Oceans in summer 2012. J. Radioanal. Nucl. Chem. 307 https://doi.org/10.1007/s10967-015-4439-0.

Kumamoto, Y., Aoyama, M., Hamajima, Y., Nagai, H., Yamagata, T., Kawai, Y., Oka, E., Yamaguchi, A., Imai, K., Murata, A., 2017. Fukushima-derived radiocesium in the western North Pacific in 2014. J. Radioanal. Nucl. Chem. 311, 1209–1217. https://doi.org/10.1007/s10967-016-5055-3.

Kumamoto, Y., Yamada, M., Aoyama, M., Hamajima, Y., Kaeriyamae, H., Nagai, H., Yamagata, T., Murataa, A., Masumoto, Y., 2019. Radiocesium in North Pacific coastal and offshore areas of Japan within several months after the Fukushima accident. J. Environ. Radioact. 198, 79–88. https://doi.org/10.1016/j.jenvrad.2018.12.015.

Kwon, E.Y., Deutsch, C., Xie, S.-P., Schmidtko, S., Cho, Y.-K., 2016. The North Pacific oxygen uptake rates over the past half century. J. Clim. 29, 61–76. https://doi.org/10.1175/JCLI-D-14-00157.1.

Kyodo News, 2018. Seven years on, radioactive water still flows into the water, study finds. The Japan Times. March 29 2018. https://www.japantimes.co.jp/news/2018/03/29/national/seven-years-radioactive-water-fukushima-plant-still-flowing-ocean-study-finds/#.XHLlJpNKigA.

Livingston, H.D., Povinec, P.P., 2000. Anthropogenic marine radioactivity. Ocean Coast Manag. 43, 689–712.

MARIS, 2019. Marine information System. International Atomic Energy Agency, Monaco. https://www.iaea.org/resources/databases/maris.

Mecking, S., Warner, M.J., 2001. On the subsurface CFC maxima in the subtropical North Pacific thermocline and their relation to mode waters and oxygen maxima. J. Geophys. Res. 106, 2156–2202. https://doi.org/10.1029/2001JC000846.

Men, W., He, J., Wang, F., Wen, Y., Li, Y., Huang, J., Yu, X., 2015. Radioactive status of seawater in the northwest Pacific more than one year after the Fukushima nuclear accident. Sci. Rep. 5 https://doi.org/10.1038/srep07757.

MEXT, 2011. Japanese ministry of education, sports, Science and technology. Available at: http://radioactivity.mext.go.jp/en/1750/2011/08/1750_083014.pdf.

Nie, X., Gao1, S., Wang, F., Qu, T., 2016. Subduction of North Pacific Tropical Water and its equatorward pathways as shown by a simulated passive tracer. J. Geophys. Res. Oceans. https://doi.org/10.1002/2016JC012305.

NSCJ, 2011. Nuclear Safety Commission of Japan: trial estimation of emission of radioactive materials (I-131, Cs-137.into the atmosphere from Fukushima Dai-ichi nuclear power station. Tokyo. Available at: http://www.nsc.go.jp/NSCenglish/geje/2011, 0412 press.pdf.

Oka, E., Qiu, B., 2012. Progress of North Pacific mode water research in the past decade. J. Oceanogr. 69, 5–20.

Oka, E., Suga, T., 2005. Differential formation and circulation of North Pacific central mode water. J. Phys. Oceanogr. 35, 1997–2011.

Oka, E., Talley, L.D., Suga, T., 2007. Temporal variability of winter mixed layer in the mid- to high-latitude North Pacific. J. Oceanogr. 63, 293–307.

Oka, E., Kouketsu, S., Toyama, K., Uehara, K., Kobatashi, T., Hosoda, S., Suga, T., 2011. Formation and subduction of Central Mode Water based on profiling float data, 2003–08. J. Phys. Oceanogr. 41, 113–129. https://doi.org/10.1175/2010JPO4419.1.

Oka, E., Qiu, B., Takatani, Y., Enyo, K., Sasano, D., Kosugi, N., Ishii, M., Nakano, T., Suga, T., 2015. Decadal variability of Subtropical Mode Water subduction and its impact on biogeochemistry. J. Oceanogr. 71, 389–400. https://doi.org/10.1007/s10872-015-0300-x.

ORO, 2013. Our Radioactive Ocean. Center for Marine and Environmental Radiation, Woods Hole, MA. http://www.ourradioactiveocean.org/.

Pike, S.M., Buesseler, K.O., Breier, C.F., Dulaiova, H., Stastna, K., Šebesta, F., 2012. Extraction of cesium in seawater off Japan using AMP-PAN resin and quantification via gamma spectroscopy and inductively coupled mass spectrometry. J. Radioanal. Nucl. Chem. https://doi.org/10.1007/s10967-012-2014-5.

Povinec, P.P., Hirose, K., Aoyama, M., 2012. Radiostrontium in the western North Pacific: characteristics, behavior, and the Fukushima impact. Environ. Sci. Technol. 46 https://doi.org/10.1021/es301997c.

Qiu, B., Hacker, P., Chen, S., Donohue, K.A., Watts, D.R., Mitsudera, H., Hogg, N., Jayne, S.R., 2006. Observations of the Subtropical mode water evolution from the Kuroshio extension System Study. J. Phys. Oceanogr. 36, 457–473.

Qu, T., Mitsudera, H., Qiu, B., 2001. A climatological view of the Kuroshio/Oyashio System East of Japan. J. Phys. Oceanogr. 31, 2575–2589.

Rainville, L., Jayne, S.R., Cronin, M.F., 2014. Variations of the North Pacific subtropical mode water from direct observations. J. Clim. 27, 2842–2860. https://doi.org/10.1175/JCLI-D-13-00227.1.

Rossi, V., Sebille, E.V., Gupta, A.S., Garçon, V., England, M.H., 2013. Multi-decadal projections of surface and interior pathways of the Fukushima Cesium-137 radioactive plume. Deep-Sea Res. I. 80, 37–46.

Rossi, V., Van Sebille, E., Sen Gupta, A., Garçon, V., England, M.H., 2014. Corrigendum to "Multi-decadal projections of the surface and interior pathways of the Fukushima Cesium-137 radioactive plume. Deep Sea Res. I 93, 162–164. https://doi.org/10.1016/j.dsr.2014.08.007.

Rypina, I.I., Jayne, S.R., Yoshida, S., Macdonald, A.M., Douglass, E., Buesseler, K.O., 2013. Short-term dispersal of Fukushima-derived radionuclides off Japan: modeling efforts and model-data intercomparison. Biogeosciences 10, 1517–1550. https://doi.org/10.5194/bgd-10-1517-2013.

Rypina, I.I., Jayne, S.R., Yoshida, S., Macdonald, A.M., Douglass, E., Buesseler, K.O., 2014. Drifter-based estimate of the 5-year dispersal of Fukushima-derived radionuclides. J. Geophys. Res. 119, 8177–8193. https://doi.org/10.1002/2014JC010306.

Saito, H., Suga, T., Hanawa, K., Watanabe, T., 2007. New type of pycnostad in the western subtropical-subarctic transition region of the North Pacific: transition region mode water. J. Oceanogr. 63, 589–600.

Saito, H., Suga, T., Hanawa, K., Shikama, N., 2011. The transition region mode water of the North Pacific and its rapid modification. J. Phys. Oceanogr. https://doi.org/10.1175/2011JPO4346.1.

Šebasta, F., 1997. Composite sorbents of inorganic ion-exchangers and polyacrylonitrile binding matrix-I. Methods of modification of properties of inorganic ion-exchangers for application in column packed beds. J. Radioanal. Nucl. Chem. 1, 77–88.

Smith, J.N., Brown, R.M., Williams, W.J., Robert, M., Nelson, R.N., Moran, S.B., 2015. Arrival of the Fukushima radioactivity plume in North American continental waters. Proc. Natl. Acad. Sci. Unit. States Am. 112 (5), 1310–1315. https://doi.org/10.1073/pnas.1412814112.

Smith, J., Rossi, V., Buesseler, K., Cullen, J., Cornett, J., Nelson, R., Macdonald, A., Marie, R., Kellogg, J., 2017. Time series measurements of the transport of the Fukushima radioactivity plume through the northeast Pacific Ocean. Environmental Science & Technology. https://doi.org/10.1021/acs.est.7b02712.

Steinhauser, G., Brandl, A., Johnson, T.E., 2014. Comparison of the Chernobyl and Fukushima nuclear accidents: a review of the environmental impacts. Sci. Total Environ. 470–471, 800–817.

Stohl, A., Seibert, P., Wotawa, G., Arnold, D., Burkhart, J.F., Eckhardt, S., Tapia, C., Vargas, A., Yasunari, T.J., 2012. Xenon-133 and caesium-137 releases into the atmosphere from the Fukushima Dai-ichi nuclear power plant: determination of the source term, atmospheric dispersion, and deposition. Atmos. Chem. Phys. 12, 2313–2343.

Suga, T., Hanawa, K., 1995. The subtropical mode water circulation in the North Pacific. J. Phys. Oceanogr. 25, 958–970.

Suga, T., Motoki, K., Aoki, Y., Macdonald, A.M., 2004. The North Pacific climatology of winter mixed layer and mode waters. J. Phys. Oceanogr. 34 (1), 3–22, 2004.

Taguchi, B., Schneider, N., 2014. Origin of decadal-Scale, Eastward-Propagating heat content anomalies in the North Pacific. J. Clim. 27, 7568–7586. https://doi.org/10.1175/JCLI-D-13-00102.1.

Talley, L.D., 1988. Potential vorticity distribution in the North Pacific. J. Phys. Oceanogr. 27, 89–106.

Tazoe, H., Obata, H., Tomita, M., Nomura, S., Nishioka, J., Yamagata, T., Karube, Z., Yamada, M., 2017. Novel method for low level Sr-90 activity detection in seawater by combining oxalate precipitation and chelating resin extraction. Geochem. J. 51, 193–197. https://doi.org/10.2343/geochemj.2.0441.

TEPCO, 2011. Tokyo electric power Company:. http://www.tepco.co.jp/en/press/corp-com/release.

TEPCO, 2017. Tokyo electric power Company:. http://www.tepco.co.jp/en/nu/fukushima-np/f1/smp/index-e.html.

Tsubono, T., Misumi, K., Tsumune, D., Bryan, F.O., Hirose, K., Aoyama, M., 2016. Evaluation of radioactive cesium impact from atmospheric deposition and direct release fluxes into the North Pacific from the Fukushima Daiichi nuclear power plant. Deep-Sea Res. I. 115, 10–21.

Tsumune, T., Aoyama, M., Tsubono, T., Misumi, K., Tateda, Y., 2017. Estimations of direct release rate of 137Cs and 90Sr to the ocean from the Fukushima Dai-ichi Nuclear Power Plant for five-and-a-half years. Geophys. Res. Abstr. 19. EGU2017-12202, 2017 EGU General Assembly, Vienna Austria.

United Nations, 2000. Exposures to the public form man-made sources of radiation. In: Sources and Effects of Ionizing Radiation. United Nations Scientific Committee on the Effects of Atomic Radiation, UNSCEAR 2000 Report to the General Assembly, with Scientific Annexes, vol. 1. U. N., New York, pp. 158–291.

Whalen, C.B., Talley, L.D., MacKinnon, J.A., 2012. Spatial and temporal variability of global ocean mixing inferred from Argo profiles. Geophys. Res. Lett. 39, L18612. https://doi.org/10.1029/2012GL053196.

Yoshida, S., Macdonald, A.M., Jayne, S.R., Rypina, I.I., Buesseler, K.O., 2015. Observed eastward progression of the Fukushima ^{134}Cs signal across the North Pacific, *Geophys. Res.* Lett. https://doi.org/10.1002/2015GL065259.

You, Y., Suginohara, N., Fukasawa, M., Yasuda, I., Kanekos, I., Yoritaka, H., Kawamiy, M., 2000. Roles of the Okhotsk Sea and Gulf of Alaska in forming the North Pacific intermediate water. J. Geophys. Res. 95, 3253–3280.

Further reading

Smith, W.H.F., Sandwell, D.T., 1997. Global seafloor topography from satellite altimetry and ship depth soundings. Science 277, 1957–1962.